

# CONTENTS

<b>1 Enhanced FCS by a Gold Nanorod in Lipid Bilayers</b>	<b>1</b>
1.1 Introduction . . . . .	2
1.2 Methods . . . . .	4
1.3 Results and discussion . . . . .	6
1.4 Conclusion . . . . .	12
1.5 Supporting Info . . . . .	14
<b>2 Dynamic Heterogeneity in Single Electron-Transfer-Proteins</b>	<b>23</b>
2.1 Introduction . . . . .	23
2.2 Experimental Section . . . . .	23
2.3 Results and discussion . . . . .	27
2.4 Conclusion . . . . .	34
2.5 Supporting Info . . . . .	36
References . . . . .	45



# 1

## ENHANCED FCS BY A GOLD NANOROD IN LIPID BILAYERS

*Plasmonic fluorescence enhancement is used to study fluorescence correlation spectroscopy (FCS) at higher concentrations than in regular diffraction-limited FCS experiments. Previous studies suffered from sticking to the substrate and were performed mainly with poorly emitting dyes. A lipid bilayer forms a passivating surface preventing sticking of the dye or the protein and allows for specific anchoring of probe molecules. For dyes with high quantum yields, the fluorescence background of unenhanced molecules is high, and the fluorescence enhancement is weak, less than about 10. Nonetheless, we show that FCS is possible at micromolar concentrations of the probe molecule. Enhanced FCS is recorded by selecting signals on the basis of their shortened lifetime. This selection enhances the contrast of the correlation by more than an order of magnitude. The lipid bilayer can be used to anchor biomolecules and perform enhanced FCS, as we show for a dye-labeled protein.*

## 1

## INTRODUCTION

Fluorescence-based single-molecule detection helps exploring the structure and dynamics of complex biological matter.[1, 2] Single-molecule signals can reveal a transient state during a chemical reaction, or report on the kinetics of processes as a function of position. Broadly there are two ways of studying single molecules: i) by immobilizing the molecule on a backgroundfree matrix or surface, ii) by dissolving the molecules in a fluid and measuring the signal fluctuation by fluorescence correlation spectroscopy (FCS).[3] Both techniques require the molecule to possess a high quantum yield and good photostability. FCS studies are limited to concentrations in the pico- to nano-molar range, in view of the diffraction-limited detection volume of a few femtoliters (fL). As many biological reactions occur in the micromolar range[4], smaller detection volumes are desirable to study these reactions by FCS.

Plasmonic nanostructures can both enhance molecular fluorescence in volumes smaller than the diffraction-limited volume and reduce the background fluorescence of the other molecules in the diffraction-limited volume. Zero-mode waveguides and antennas-in-box, in particular, both enhance fluorescence and reduce background.[5–9] The effective fluorescence enhancement depends sensitively on the position and orientation of the molecule with respect to the nanoparticle. It originates from two factors, excitation enhancement and radiative enhancement. By confining the optical field into so-called hot spots with volumes much smaller than the diffraction limit,[10] plasmonic nanostructures enhance the incident field by up to a few orders of magnitude, leading to excitation enhancement.[8, 11–16] They also alter the radiative and non-radiative decay rates of molecules in their vicinity. The ensuing radiative enhancement results from improved emission by the nanoantenna dipole induced by the molecular dipole. In addition, energy may be transferred from the molecule to the antenna resulting in non-radiative losses and energy dissipation in the metal. Changes in the radiative or non-radiative decay paths lead to altered, generally shortened fluorescence lifetimes.[16–22] Distance-dependent lifetime measurements show lifetime shortening up to 40 nm away from the metal surface.[20]

Noble-metal plasmonic nanostructures can be fabricated either by lithography or by colloid chemistry.[23] Whereas lithography can produce nanostructures with arbitrary geometries suitable for high optical confinement, it presents the disadvantages of complex processing, polycrystallinity, surface roughness, and high cost. Colloidal chemistry produces large numbers of highly crystalline nanostructures in a few basic shapes (spheres, rods, bipyramids, etc.) that are controllable to some extent, at a low cost. Among the basic nanoparticle shapes, nanorods[8] can be just as efficient as lithographically-made structures[7, 12] in enhancing fluorescence. Gold nanorods confine the optical field more weakly than lithographically made gap structures, but they have the advantage of a narrow surface plasmon resonance, which can be tuned in the red and near infrared range by changing the rods' aspect ratio.[16] The largest enhancement is achieved for a maximum overlap of the molecule's excitation and fluorescence spectra, of the nanorod's surface plasmon resonance, and of the excitation wavelength. Further advantages of gold nanoparticles are that they provide easy access of hot spots to diffusing molecules and that they can be inserted into complex environments such as living cells.

Confinement of light in volumes much smaller than the diffraction-limited volume

combined with fluorescence enhancement open applications of FCS at micromolar dye concentrations. The correlation contrast in FCS decays as the square of the background intensity. To reduce background, most enhanced FCS experiments have been done on dyes with low quantum yields.[6, 24] Alternatively, a fluorescence quencher may be added to a dye with a high quantum yield (QY) to reduce background.[7, 9] A metal box or cladding[25] can also be fabricated around the nano structure to improve the correlation contrast against the background of unenhanced molecules. Both solutions have disadvantages, as a millimolar quencher concentration may be harmful to a living cell. Metal claddings are difficult to fabricate and to manipulate in a complex environment. Generalizing enhanced FCS to high-QY dyes would obviate these two problems and open plasmonic enhancement to biological marker dyes, most of which have high QY. Plasmonic enhancement may also help overcome other background sources such as autofluorescence in live-cell experiments. Indeed, as we show herein, even weak fluorescence enhancements suffice to overcome background in FCS experiments. Moreover, fluorescence photons with short emission times may be selected as was done by Acuna et al[13] further to improve the signal to noise ratio of enhanced FCS.

A further limitation in working with metal nanostructures on a solid substrate is the nonspecific interaction of the molecules with metal and substrate, which not only may affect the molecules' functionality but also make measurements troublesome.[6, 8, 26] Micellar solutions have been used to minimize sticking but are not ideal when studying biomolecules or performing experiments in live cells. We therefore need to suppress or mitigate nonspecific interactions of the dyes or biomolecules under study with the solid substrates supporting the structures. Living organisms use a lipid bilayer on their outer surface to prevent nonspecific interaction and protein fouling while allowing specific binding of membrane proteins.[26, 27] We have used a supported lipid bilayer to passivate the substrate.[28–30] Supported bilayer can be self-assembled on solid surfaces (glass, silica, and similar polar surfaces) such that it forms a single, continuous membrane which possesses a high degree of lateral mobility by maintaining a very thin layer of water (1 nm) between substrate and bilayer.[31–34] Bilayers are also model systems to study diffusion in biological membranes. In standard experiments, diffusion in bilayers is studied on length scales limited by far-field resolution. Plasmonic enhancement gives us access to diffusion on the length scales of the near field, typically some tens of nm. Enhanced fluorescence experiments provide access to nanoscale diffusion in the vicinity of a gold nanorod.

Here we study fluorescence enhancement of a high-QY dye by immobilized single gold nanorods. Sticking of the dye to the glass substrate was prevented by coating the glass with a supported lipid bilayer formed from a zwitterionic lipid. We have characterized the properties of the enhanced signal and shown that its fluorescence decay is much faster than the far-field signal's. Based on these time decay characteristics, we have filtered the near-field signal from the background of unenhanced dye fluorescence, thereby obtaining an improved FCS contrast. The same measurement provides both far-field and near-field diffusion components, and allows us to compare the diffusion kinetics in both regimes. We show that biomolecules can be successfully anchored in the bilayer, and that enhanced FCS can be performed while sticking and interaction with gold nanorods are prevented.

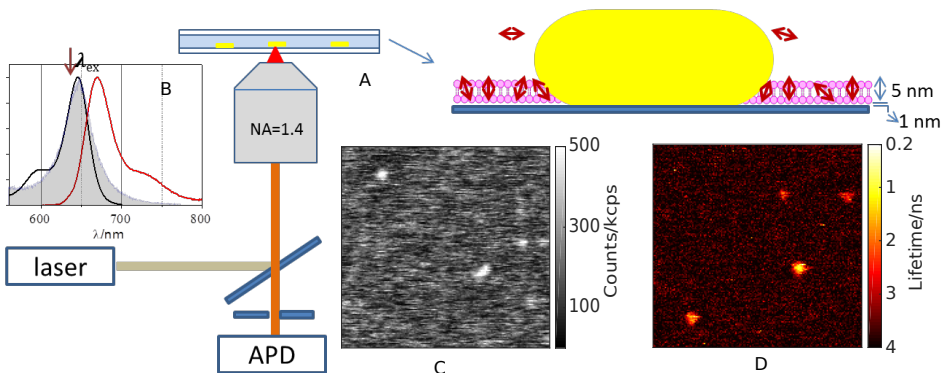


**Figure 1.1.** (A) Schematic diagram of the optical setup with a supported lipid bilayer (pink), ATTO 647N molecules (red) and a gold nanorod (yellow). (B) Absorption spectrum of ATTO 647N (black), fluorescence spectrum of ATTO 647N (red) and photoluminescence spectrum of a single gold nanorod (shaded area). Notice the overlap of the nanorod's SPR with the dye's absorption and emission spectra. (C) fluorescence intensity image (size  $8\text{ }\mu\text{m} \times 8\text{ }\mu\text{m}$ ) and (D) fluorescence lifetime image (FLIM) of the same area of lipid bilayer. Note the lack of correlation between the fluorescent spots indicating dye aggregates in (C) and the short-lifetime spots in (D) indicating the rods.

## METHODS

**Gold nanorod immobilization.** Gold nanorods (AuNRs) were synthesized in cetyl trimethyl ammonium bromide (CTAB) using the seed-mediated growth method.[35] The average dimension of the nanorods was  $90\text{ nm} \times 50\text{ nm}$ . Fig. S1.7B shows a scanning electron microscopy image of the nanoparticles. The bulk absorption spectra of these nanorods in Fig.S1.7A show the longitudinal surface plasmon resonance (LSPR) at 640 nm. The nanorod sample was diluted and the CTAB was washed away by centrifugation and re-suspension in milliQ water before use. Glass coverslips (Menzel-Glaser, 22 mm × 40 mm, no. 1 thickness) were used for immobilization. The coverslips were sonicated in water (15 min) and acetone (15 min). Then they were rinsed in milliQ water several times and incubated in a  $\text{H}_2\text{O}/\text{NH}_4\text{OH}/\text{H}_2\text{O}_2$  (5:1:1) bath at 70 °C. The coverslips were rinsed several times with water and ethanol, and finally stored in ethanol. Before use the coverslips were flamed, and then ozone-cleaned for 15 min. The nanorods were spin-coated onto these coverslips at 2000 rpm for 1 min. These parameters gave us around 5 particles per  $100\text{ }\mu\text{m}^2$  area and more than 90 % of them were single. The coverslips with the gold nanorods were then rinsed with water to remove remaining traces of CTAB, dried, and again ozone-cleaned for 30 min. This resulted in a very hydrophilic surface. The cover-slip was mounted in a homemade flow cell, where the surface was further prepared for confocal experiments.

**Supported lipid bilayer preparation.** Supported lipid bilayers were prepared from a zwitterionic lipid. Stock ampoules (25 mg) of 1-palmitoyl-2-oleoyl-sn-glycero-3 phosphocholine (POPC, see Fig.SrefS1fig:chemicalB) were purchased from Avanti polar and stored at -20 °C immediately after receipt. The lipid powders were dissolved in chlo-

roform and dried with argon in glass vials 1 mg each and again stored at -20 °C until required. 4 ml of Phosphate Buffered Saline (PBS) were added to the glass vial and the POPC was incubated for 1 h at 40 °C (which gives a concentration of 0.25 mg ml<sup>-1</sup>). Then the vial was placed in the middle of a sonicator where the cavitation is greatest. It was sonicated for 30 min to produce small unilamellar vesicles (SUVs). The coverslips in the flow cell were hydrated by flowing PBS into the cell for 5 min. Then the coverslip was incubated with the SUV sample for 1 h and washed with PBS to remove all free vesicles and debris. The vesicles rupture, spread and form a bilayer.<sup>[34]</sup> For protein anchoring, the vesicles for the bilayer were prepared from a mixture of POPC and DSPE-PEG(2000) Biotin (See Fig. S1.8C) with a ratio of 100:1.

**Labeling of the bilayer.** ATTO 647N NHS-ester (see Fig. S1.8 for the structure) was purchased from ATTO-TEC. Before labeling, the reactive part of the dye (NHS-ester) was neutralized by incubating in 20 mM Tris buffer pH 9 (the amine group present in Tris reacts with the ester). The dye in Tris pH 9 buffer at the concentration required by the experiment (vide infra) was passed into the flow cell. The dye goes into the bilayer only at higher pH probably because of the neutralization of charge on the nitrogen atom present on the head group of the lipid molecules. The dye mentioned in the whole discussion is ATTO 647N unless otherwise stated.

**Protein to bilayer anchoring** Wild type (wt) azurin was prepared, purified and labeled as previously described.<sup>[36, 37]</sup> ATTO 655 NHS ester was incubated with the azurin and azurin labeled at Lys122 was isolated and purified by chromatography on a MONO Q anion exchange column. Biotin-PEG-NHS (MW 3400, LaysanBio) was reacted with other lysine groups in the protein and the unreacted linkers were removed by centrifugal filtration. This labeled protein was then used for binding to the bilayer. A glass slide with a bilayer containing DSPE-PEG Biotin was incubated in a flow cell with neutravidin for 30 min and then washed with fresh PBS buffer. A 5 nM solution of the labeled protein was flushed into the flow cell and left for 15 min and then the cell was washed again to remove the unbound proteins.

**Optical setup** Measurements were carried out in a home-built confocal microscope. A 639 nm pulsed laser was controlled by PDL 800-B (PicoQuant) at 20 MHz repetition rate. This laser was used to excite the dye. A 632 nm Nd:YAG laser was used to measure the spectra of the gold nanorods. The 639 nm beam was passed through a narrow-band clean-up filter (LD01-640/8-25, Semrock) and coupled into a single-mode fiber (OZ optics). After passing the fiber the beam was collimated and passed through a quarter-wave plate to evenly excite nanorods irrespective of their orientation on the flat glass surface. The beam was reflected by a dichroic mirror (ZT640RDC, Chroma for 639 nm and T556lpxr-UF1 for 532 nm and entered an oil immersion objective with numerical aperture (NA) of 1.4 (100X-oil, Zeiss) which focused it to a diffractionlimited spot of 265 nm beam waist. The flow cell with the coverslip was mounted on a scanning stage controlled by nano-positioning piezo elements (P517.3CD, Physik Instrumente). The formation of the bilayer and its labeling were performed on this scanning stage and measurements were performed in each step. The epifluorescence was collected by the same objective

and was separated from the excitation laser through an emission filter (ET655LP, Chroma for 639 nm laser) or notch filter (NF01-532U-25, Semrock for 532 nm laser). The emission was then spatially filtered by a 75  $\mu\text{m}$  pinhole and focused on a single-photon-counting module (SPCM-AQR-14, Perkin Elmer). The data were recorded through a photon counting PC-board (TimeHarp 200, PicoQuant) in time-tagged-time-resolved mode. The data acquisition and analysis were performed by using SymPhoTime (PicoQuant) software.

**Image and time trace recording** The mounted sample was brought into focus and a typical area of  $100 \mu\text{m}^2$  was imaged. The laser was parked on a gold nanorod and luminescence spectra were measured with a spectrograph equipped with a nitrogen-cooled CCD camera (Princeton Instruments SPEC-10). We made sure that the nanorods are single by verifying that the line shape of the luminescence spectrum was Lorentzian (Fig. 1.1b, shaded area). A tris-neutralized solution of 50 pM and 100 nM ATTO 647N in Tris pH 9 was introduced into the flow cell. The sample was imaged in both XZ and XY planes. The luminescence intensity of the gold nanorods was not high enough to be distinguishable from the background. As the lifetime of the gold nanorod luminescence is much shorter than that of ATTO 647N (vide infra), fluorescence lifetime imaging (FLIM) was used to spot the nanorods (Fig. 1.1D). Time traces were recorded in time-tagged-time-resolved mode at a power of 0.5  $\mu\text{W}$  for burst analysis and 0.1  $\mu\text{W}$  for FCS and were further analyzed with Symphotime software. To compare far-field and near-field, the laser was parked either on a gold nanorod or on the bilayer-covered glass surface.

## RESULTS AND DISCUSSION

To estimate the enhancement factor of single molecules, we flushed a 50 pM solution of ATTO 647N into the flow cell and allowed the dye to partition between solution and lipid bilayer, where diffusion is much slower. At this concentration we have less than 0.04 molecules in our diffraction-limited volume of 0.5fL, making sure that the probability of observing more than one molecule in the far field at any time is very low. Figure 1.2A shows a time trace of the gold nanorod in the absence of the dye. The intensity of the gold nanorod luminescence is around 50 kcps. ATTO 647N in the bilayer far away from nanorod shows peaks with an intensity of around 100 kcps as shown in Fig 1.2C. The time trace and count histogram of ATTO 647N in the bilayer around a nanorod shows higher intensity bursts with a maximum intensity of around 460 kcps. By subtracting the nanorod luminescence intensity, we get a maximum of 410 kcps (Fig. 1.2E) intensity which gives us a factor of four enhancement in the fluorescence. Histograms of photon counts per time bin of 100  $\mu\text{s}$  are presented for each time trace in Fig. 1.2B, D, E. They show a much more intense tail of bright events for the enhanced trace in the presence of the rod, as observed previously.<sup>[16]</sup> Figure 1.3 presents four examples of time traces zoomed in around fluorescence bursts (Fig. 1.3C) together with schemes qualitatively explaining the observed traces. Several combinations of far-field and near-field trajectories were observed. Fig 1.3a (blue trace a) shows a molecule passing through the far-field without crossing the near field, the most probable event. Once in a while, a molecule passes from the far field to the near field (red b and magenta d) resulting in enhanced fluorescence. This is consistent with the enhancing hot spot being surrounded by the

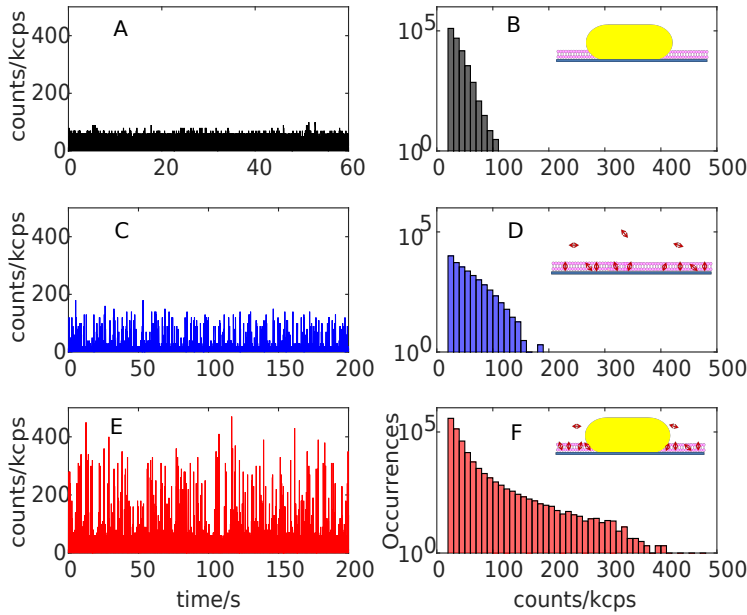


**Figure 1.2.** Enhanced Fluorescence by a gold nanorod in a bilayer. Fluorescence time traces with binning time  $100\mu\text{s}$ . (A) Time trace of a gold nanorod in the absence of the dye, (C) Time trace with  $50\text{ pM}$  ATTO 647N in the bilayer (E) Time trace with  $50\text{ pM}$  ATTO 647N in the bilayer in presence of the gold nanorod. The corresponding histograms of counts are shown to the right of each time trace (B, D, F).

far-field spot. In a few rare cases, a molecule starts directly from the near-field (green c) and diffuses away through the far field. We attribute this sudden appearance to adsorption of a molecule from the solution (where it diffuses too fast to be visible) to the bilayer in the near-field area. Indeed, the dye being partly soluble in water and in the bilayer, it partitions in a dynamical equilibrium between the two phases. More examples of such bursts, including near-field traces suddenly interrupted by desorption or bleaching are described and briefly discussed in the Supporting Information (paragraph\* 4). The four-fold enhancement found above for a high-QY dye in the bilayer is much lower than the enhancements observed earlier for poorly emitting dyes.<sup>[8]</sup> We ascribe this lower enhancement to reductions of both excitation and emission enhancements in our present case. We first consider the position of the dye molecules with respect to the rod's tips. Because the dyes in the bilayer are confined in a  $5\text{ nm}$  thick layer that is assumed to stick onto the glass substrate, they are largely outside the near-field hot spots at the tip of the  $50\text{ nm}$  wide nanorod (see sketch in Fig.1.1), and are thus unable to explore the region of the hot spot with the highest intensity, resulting in a lower excitation enhancement than with 3D diffusion. Indeed, we observed a much higher enhancement of ATTO 647N when the molecules were allowed to explore the whole space in 3D solution around the gold nanorod (see Supporting Fig.S1.15; in this latter experiment, sucrose was added to the solution to match the diffusion constant with that in the bilayer). Secondly, the

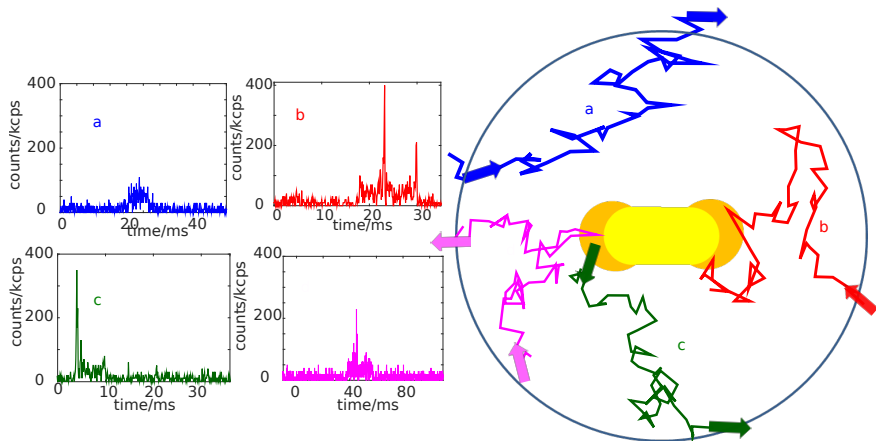


**Figure 1.3.** Dye trajectories. (Left part) Different types of near-field enhanced intensity time traces observed in presence of the gold nanorod. (Right part) Schematic interpretation of the traces on the left, with molecules entering, leaving and diffusing in the far-field and near-field zone around an illuminated gold nanorod. The colors of the schematic trajectories correspond to the colors of time traces. Blue: The molecule enters and leaves the far-field without passing through the near field; Red: the molecule enters the far-field area via the bilayer, crosses the near field twice and either bleaches or desorbs to the solution; Green: The molecule enters the near field from the solution and leaves via the far-field; Pink: the molecule enters the far field from the bilayer, crosses the near field, and finally leaves the far field again via the bilayer.

emission enhancement is much reduced compared to low-quantum yield dyes. Indeed, as the radiative channel of ATTO 647N (quantum yield 65 %) is not competing with a strong nonradiative channel, the emission yield can at best be increased up to 100 %, by a factor of only 1.5.[16] The time traces presented in Figure 1.2A-E were further analyzed to obtain lifetimes. Histograms of arrival times of photons are presented in Figure 1.4. The lifetimes were obtained taking the instrument response function into account. The black time trace shows the photo luminescence of the rod in the absence of dye. As the luminescence lifetime is very short, the associated lifetime histogram (black) reproduces the instrument response function. For the pure dye in the absence of the rod, we find the usual bursts (Figure 1.2C) as seen in standard FCS, and the associated decay is single exponential with a lifetime of 3.7 ns (blue). The enhanced fluorescence time trace of rod with dye (red) gives rise to a nonexponential histogram, including a short response from the rod luminescence and a second component which resembles the free dye decay. Lastly, we applied a threshold of 120 kcps to select enhanced bursts in the time trace of ATTO 647N in the presence of the rod. The associated histogram (in green) is nonexponential. This decay shows a strong lifetime reduction compared to the free dye. The decay of enhanced fluorescence is always faster than that of unenhanced fluorescence. We attribute this shortened lifetime to a combination of both emission enhancement and fluorescence quenching. Although we did not attempt to quantify the radiative and non-radiative effects on the dye, in the coming paragraph's we can still use the lifetime and intensity to discriminate between enhanced photons and photons from the unen-

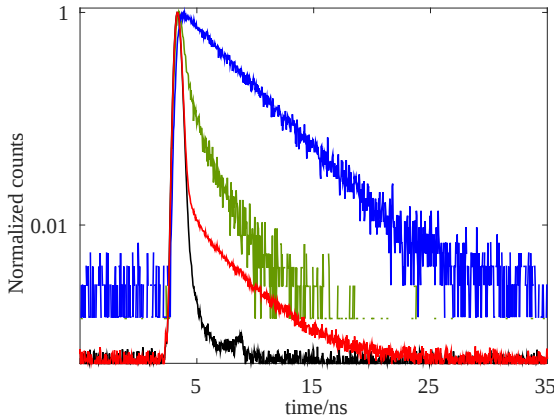


**Figure 1.4.** Fluorescence Decay. Normalized fluorescence decay of: ATTO 647N only (blue), ATTO 647N in presence of gold nanorod (red), events from intensity bursts with more than 120 kcps (green), nanorod luminescence (black)

hanced background.

To perform fluorescence correlation spectroscopy (FCS), we prefer to increase the number of dye molecules in the confocal volume. To this end, we incubated the bilayer with a solution of 100 nM ATTO 647N on the bilayer (See Fig. 1.1C). Because of the high background and the presence of dye aggregates from un-ruptured vesicles, the identification of gold nanorods is difficult. As the lifetime of enhanced fluorescence and of nanorod luminescence is much shorter than that of ATTO 647N, we applied fluorescence lifetime imaging (FLIM) to distinguish the rods. The lighter spots in the lifetime image (Fig. 1.1D) indicate nanorods, which only rarely correspond to brighter spots in the fluorescence intensity image.

The fluorescence autocorrelation function is given by  $G(\tau) = \langle I(t)I(t+\tau) \rangle / \langle I(t) \rangle^2$  and keeps track of the temporal fluctuations of the fluorescence intensity  $I(t)$  (where  $\tau$  is the lag time and ... represents time averaging). For molecules confined to the bilayer, the correlation can be fitted with a two dimensional diffusion model in a Gaussian beam:

$$G_{FF}(\tau) - 1 = \frac{1}{N_{FF}} \left( 1 + \frac{\tau}{\tau_{FF}} \right)^{-1}, \quad (1.1)$$

where  $N_{FF}$  represents the average number of molecules in the focal spot and  $\tau_{FF}$  is the diffusion time in the focal spot. The amplitude or contrast of the autocorrelation,  $[G(0) - 1]$ , directly gives the average number of fluorescent species in the detection volume,  $N_{FF} = [G(0) - 1]^{-1}$ . In presence of a nanorod, we fitted the FCS curves with the theoretical model of Langguth and Koenderink (see ref.[38] and Supporting Information Sec.5). In the model the molecule detection function is considered as the superposition of two coinciding 2D Gaussians, leading to the following correlation function:

$$G(\tau) - 1 = \frac{1}{\langle C \rangle S_{MDF}^2} \left[ \sum_n A_{nn}(\tau) + \sum_{n \neq m} A_{nm}(\tau) \right], \quad (1.2)$$

with  $n, m = F$  (far-field), or  $N$  (near-field),

$$A_{n,m}(\tau) = S_n S_m \left[ \frac{2}{\pi \left( [\omega_n]^2 + [\omega_m^D(\tau)]^2 \right)} \right], \quad (1.3)$$

$$\omega_m^D(\tau) = \sqrt{\omega_m^2 + *D\tau}, \quad S_n = P_n \times A_n \text{ and } S_{MDF}^2 = \left[ \sum_n S_n \right]^2,$$

where  $P_n$  indicates the peak intensity and  $A_n$  the area of the Gaussian distribution. The near-field width ( $\omega_N$ ) and peak intensity ratio ( $P_N = P_N/P_F$ ) were derived from the fitting. The contrast corresponding to  $A_{NN}$  term (i.e near-field/ near-field correlation) at zero lag time can be given by:

$$G_{NN}(0) = \frac{P^2 \frac{\omega_N}{\omega_F}}{N_{FF} \left( 1 + P \frac{\omega_N}{\omega_F} \right)^2}. \quad (1.4)$$

The autocorrelation of the time trace at 100 nM ATTO 647N is shown in Fig.1.5C. The blue curve corresponds to the dye diffusing in the bilayer without gold nanorod. The diffusion time in the far field  $\tau_{FF}$  is related to the beam waist  $\omega$  ( $1/e^2$  radius of the detection area which was measured to be 265 nm of the beam and to the diffusion coefficient  $D$  by  $\omega^2 = 4D\tau_{FF}$ . For ATTO 647N in the bilayer, this time as determined from a fit of the autocorrelation is  $3.95 \pm 0.05$  ms, which gives for the diffusion coefficient  $4.44 \mu\text{m}^2 \text{s}^{-1}$ . From the value of  $G_{FF}(0)$ , the average number of dye molecules in the bilayer found to be 35 at 100 nM ATTO 647N in the confocal detection area of around  $0.22 \mu\text{m}^2$ , i.e., 160 molecules/ $\mu\text{m}^2$ . The same number of molecules in the diffraction-limited spot would correspond to a threedimensional concentration of  $0.8 \mu\text{M}$ . In the presence of gold nanorods, an extra component on a smaller time scale in the autocorrelation is observed. From the red curve in Fig.1.5C, we obtained a near-field width of  $31 \pm 6$  nm, around 10 times smaller than the far-field width. The peak intensity ratio ( $P$ ) between near-field and far-field was obtained to be  $5 \pm 1.5$ .

The diffusion coefficient  $4.44 \mu\text{m}^2 \text{s}^{-1}$  obtained for ATTO 647N in the bilayer is close to the literature values of  $3\text{--}4 \mu\text{m}^2 \text{s}^{-1}$  [39] for other dyes and is similar to those of freely moving lipid molecules in the bilayer. No correlation component was observed for the dyes in the solution because of the low fluorescence intensity and high background from the dyes diffusing in the bilayer. In presence of a nanorod, we find the same long diffusion time again, corresponding to molecules diffusing in the diffraction-limited area, while we assign the shorter component to diffusion in the near-field of the gold nanorod, responsible for enhanced brightness of the molecules. The near-field width is about 10 times smaller than the far-field diameter, and is consistent with near-field simulations and lifetime calculations around gold nanorods of this size. [16, 20] The near-field area is reduced by more than one order of magnitude (70 times in our case). Assuming the diffusion coefficient to be same in the far field and near field, and applying the analysis for a Gaussian near-field intensity distribution, we obtain a diffusion time of  $57 \pm 11 \mu\text{s}$  in the near-field from the relation  $\omega^2 = 4D\tau_N$ . The peak ratio  $5 \pm 1.5$  is close to the maximum enhancement factor of 4 obtained from the burst analysis (vide supra) which confirms the results obtained in the FCS and shows that the maximum enhancement factor can simply be obtained from the FCS. However, the contrast of the near-field correlation

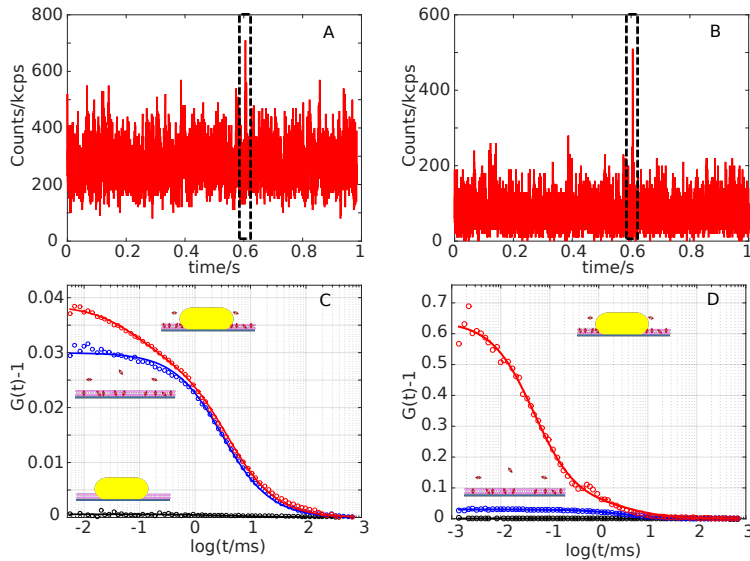


**Figure 1.5.** Fluorescence correlation in high background. Fluorescence time trace of 100 nM ATTO 647N in the presence of a nanorod before (A) and after (B) lifetime filtering. The dashed boxes highlight a near-field burst in both traces. Autocorrelations of fluorescence intensity traces at 100 nM ATTO 647N before (C) and after (D) lifetime filtering. Red circles: correlation in presence of the rod; blue circles: correlation in the absence of the rod; black circles: correlation of the gold luminescence only (in absence of ATTO 647N).

(0.01) is much weaker, which may make it difficult to distinguish this component in FCS experiments with lower signal-to-noise ratios.

As can be seen in Fig. 1.5A, C, the contrast of the near-field component is weak, essentially because it is reduced by background. To further enhance this correlation component, we can exploit a further difference between enhanced and unenhanced counts, namely their delay after excitation, less than 2 ns versus 3.7 ns, respectively. We thus filtered out unenhanced photons by selecting photons detected within 1 ns from the excitation pulse, and computed their correlation function. A typical time trace before and after filtering can be seen in Fig. 1.5 A, B. The average background went down from 272 kcps to 74 kcps and the signal-to-noise ratio of the enhanced signal improves accordingly, as can be seen for the burst marked in the box. The contrast of the near-field component in the filtered correlation has now been enhanced by about 60 times, making it easy to distinguish against the far-field correlation. From the filtered correlation in Fig. 1.5D, we find a near-field diffusion time of  $59 \pm 5 \mu\text{s}$ , similar to the one deduced from the unfiltered correlation. Shorter filtering windows lead to even shorter times for this near-field component, corresponding to larger emission enhancement and quenching at shorter distances. However, this dependence is rather slow, so that the above number has physical meaning as the typical near-field diffusion time. Of course, filtering down to very short times considerably reduces the signal-to-noise ratio (See Fig. S1.14)

The bilayer-nanorod platform can be used for biochemical applications. We demon-

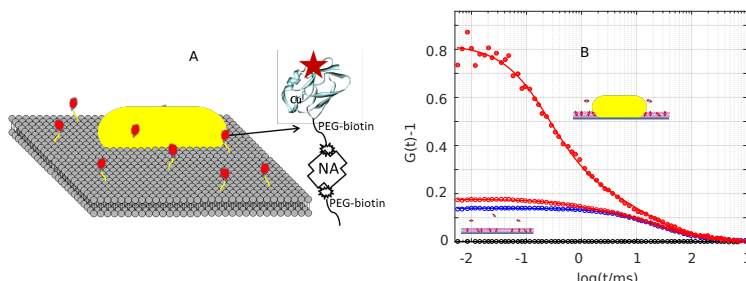


**Figure 1.6.** (A) Scheme showing the labeling strategy for protein anchoring onto the bilayer. The Azurin labeled with ATTO 655 and biotin binds to DSPE-PEG-Biotin in the bilayer through Neutravidin. (B) Autocorrelation of the time traces of the labeled protein in absence of the nanorod (blue), in the presence of the nanorod (red circles) and in the presence of the nanorod after lifetime filtering (solid red). Notice the higher correlation contrast after lifetime filtering in presence of nanorod.

strate this by anchoring a protein, azurin, onto the bilayer. This protein with a copper metal center is known to mediate electron transfer in biological redox processes.[40, 41] To prevent electron transfer processes in the present experiments, we used azurin with a zinc metal center. The protein's Lysine 122 residue was labeled with ATTO 655. As Zn-Azurin does not show electron transfer, electron transfer to or from the dye is excluded. The anchored protein shows free mobility on the bilayer as can be inferred from the single decay component of the autocorrelation (Fig.1.6B, blue). This component has a diffusion time of  $22 \pm 5$  ms in the far field, which is around five times longer than the diffusion time of the free dye ATTO 647N. We attribute this longer diffusion time to interactions and reduced mobility of the bulky anchoring among surrounding lipids. We now turn to the correlation curve in the presence of the nanorod. The absence of any long-lived correlation component indicates that the protein continues to diffuse freely and does not stick to the solid surfaces. The near-field diffusion time for the protein was found to be  $318 \mu\text{s}$ , which is also around five times the near field time of ATTO 647N. This confirms that diffusion is not significantly altered, even within 30 nm of the rod.

## CONCLUSION

A lipid bilayer substrate prevents the nonspecific sticking of dyes to a glass surface and thereby makes it possible to perform enhanced FCS around a metal structure with no hindrance in the diffusion kinetics. The fluorescence of molecules in the near field always decays faster than that of far-field molecules. The shorter lifetime of enhanced fluorescence can be used to discriminate the near-field signal from the high background in the far field. The autocorrelation of the shorter lifetime component shows spectacular improvement in the correlation contrast which is helpful for studying FCS at high concentrations in presence of a strong background from unenhanced molecules. The bilayer substrate with nanostructures can be used as a hybrid surface where probe molecules can either be functionalized to the surface or be kept free in the solution without any nonspecific interaction. As lipid bilayers are close to biological membranes, many kinds

of biochemical FCS experiments on the bilayer at physiological concentrations can be envisioned.

## SUPPORTING INFO

### Gold nanorod characterization

**Chemicals** Figure 1.8 shows the chemical structure of the dye ATTO 647N used in the experiments. The hydrophobic moiety of the molecule helps it enter the bilayer. The lipid (Figure S2B) has a zwitterionic head which helps to avoid nonspecific sticking.

**Bilayer Characterization** Figure S1.9 shows a raster-scanned image of a bilayer with 100 nM ATTO 647N in the XZ plane (perpendicular to the substrate). A higher intensity is observed at the glass-buffer interface showing the presence of dye in the bilayer. The lifetime image helps to distinguish a nanorod (blue spot on the left of Fig. 1.9B) against the background fluorescence.

A large area of the bilayer labeled with ATTO 647N can be seen in Figure S1.10A. The intensity is almost uniform across the whole area except for some bright and dark spots. The bright spots are probably un-ruptured vesicles and the dark spots indicate holes in the bilayer. Measurements described in the text have been conducted far away from these holes. The bright spots in the lifetime image (Fig.S1.10C) indicate the nanorods. Most of the bright spots in the intensity image don't correlate with the bright spots in the lifetime image. This is the reason we rely on the lifetime image to locate the gold nanorods.

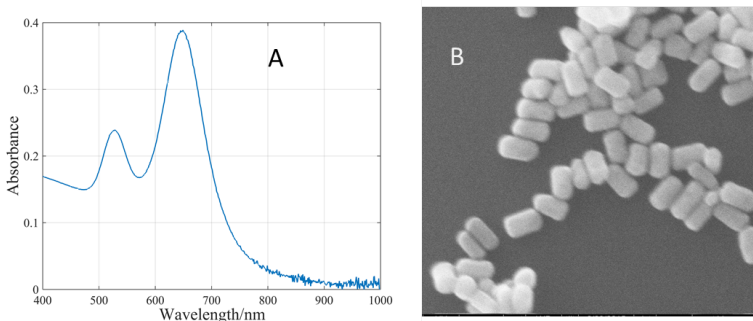


**Figure S1.7.** A, Extinction spectrum of a bulk gold nanorod suspension in water. B, Scanning electron microscope image of nanorods. The average dimensions of the nanorods are 90 nm × 50 nm.

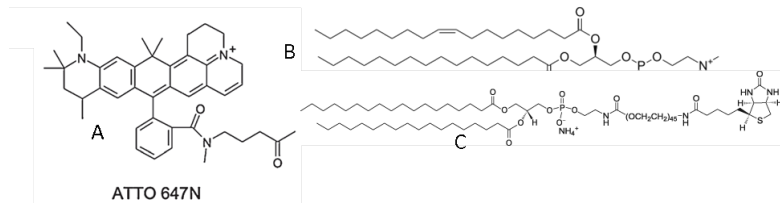


**Figure S1.8.** Chemical structure of ATTO 647N (A), POPC lipid (B), DSPE-PEG(2000)Biotin (C)

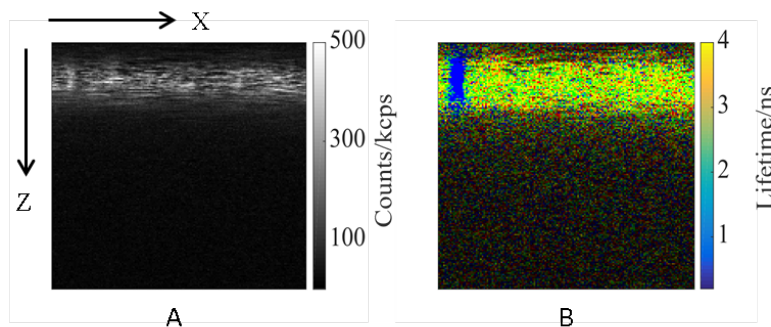


**Figure S1.9.** (A) Fluorescence intensity image (size  $8\mu\text{m} \times 8\mu\text{m}$ , and (B) fluorescence lifetime image (FLIM) both taken perpendicular to the plane of the lipid bilayer (from the glass surface at the top to the solution at the bottom). The bilayer was labeled by incubation with a solution of 100 nM ATTO 647N in Tris pH 9 buffer.

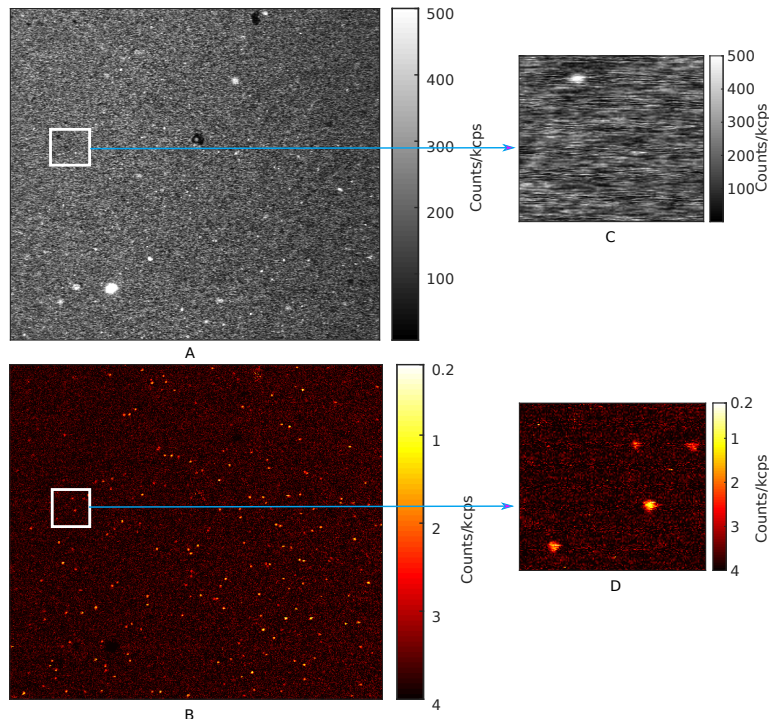


**Figure S1.10.** Intensity image (A) and lifetime image (C) of a  $80\mu\text{m} \times 80\mu\text{m}$  area of a glass substrate with spin-coated gold nanorods and covered with a supported lipid bilayer. The bilayer is labeled by incubation with  $100\text{ nM}$  ATTO 647N. Intensity image (B) and lifetime image (D) of a zoomed-in area of the original image.

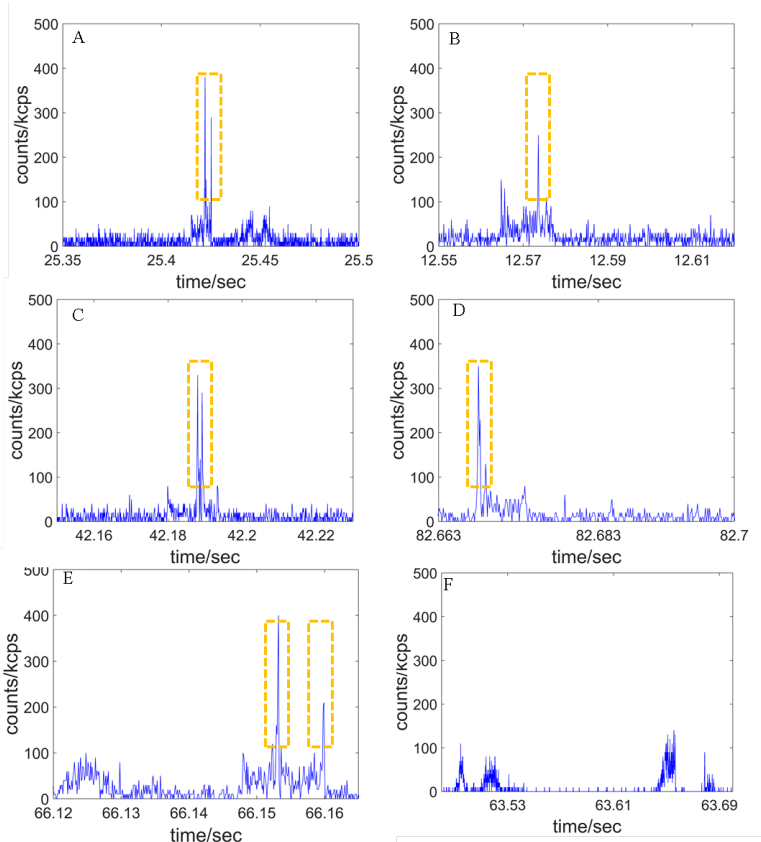


**Figure S1.11.** Zoomed-in time traces of the enhanced bursts (A-E) observed for ATTO 647N in the presence of gold nanorod showing that the enhanced signal nearly always is embedded in the far field signal; (F) Time trace of ATTO 647N in the bilayer in the absence of gold nanorod. The full time traces were shown in Figure 1.

**Zooming in on intensity bursts** Figure S1.11A-E shows different enhanced bursts observed when ATTO 647N molecules diffuse around a gold nanorod. The distinction is made on the basis of intensity. Intensity levels above 100 kcps represent enhanced signals and have been marked by a dotted box. In all the bursts shown it can be seen that the near-field signal is observed only in the presence of the far-field signal. A molecule travels some distance in the far field before it reaches the near field. In absence of gold nanorod (Fig. S1.11F), we only see the far-field signal and no short bursts, as expected.

**Fitting of FCS curves** As only probe molecules in the bilayer contribute to the signal, the FCS curves without nanorod were fitted with a two-dimensional Gaussian model:

$$G_{FF}(\tau) - 1 = \frac{1}{N_{FF}} \left( 1 + \frac{\tau}{\tau_{FF}} \right) \quad (1.5)$$

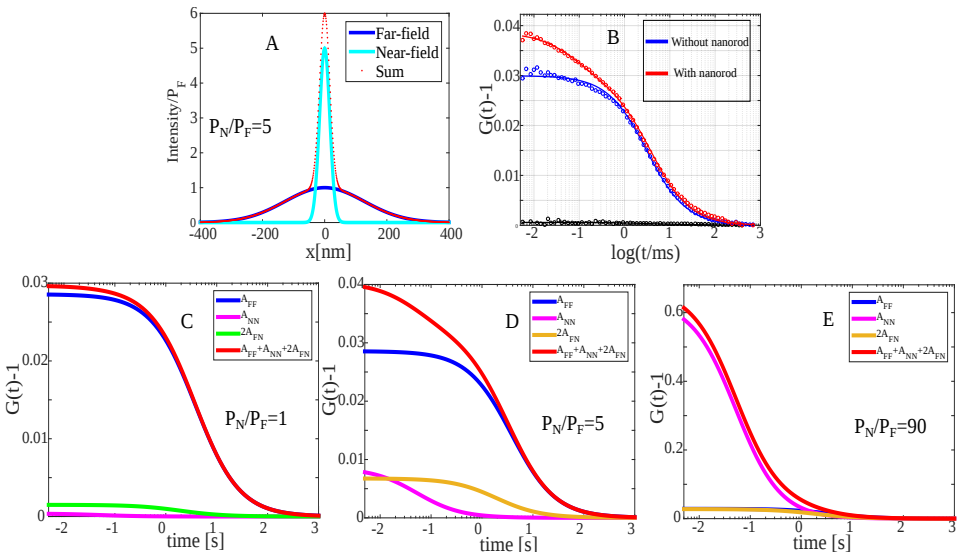


**Figure S1.12.** (A) crosscut (red dots) through an intensity profile consisting of the sum of two Gaussians: Far-field Gaussian (blue, waist=265 nm; peak height:  $P_{FF} = 1$ ) and near-field Gaussian (magenta, waist = 31 nm; peak height:  $P_{NF} = 5$ ). (B) Experimental autocorrelations of fluorescence intensity traces at 100 nM ATTO 647N in presence of the rod (red circles), in the absence of the rod (blue circles), and of the gold luminescence only (black circles, in absence of ATTO 647N). (C-E) Calculated autocorrelation for the entire intensity profile (red) and its constituents: the autocorrelation of far-field focus AFF (blue), the near-field  $A_{NN}$  (magenta) and the sum of identical cross-terms  $2A_{FN}$  (green) with different peak heights  $P_{FN}/P_{FF} = 1$  (C),  $P_{FN}/P_{FF} = 5$  (D) and  $P_{FN}/P_{FF} = 90$  (E). The calculated correlations fit best the experimental correlations for a peak height ratio of 5. This value is very close to the maximum factor of 4 enhancement obtained from direct comparison of burst intensities (main text).

where  $_{FF}$  represents the average number of molecules in the focal spot and  $\tau_{FF}$  is the diffusion time in the focal spot. The amplitude of the autocorrelation,  $G(0) - 1$  directly gives the average number of fluorescent species in the detection volume,  $N = [G(0) - 1]^{-1}$ . At incubation with a solution of 100 nM ATTO 647N in buffer, the average number of molecules in the bilayer appeared to be 35. Background corrections were negligible.

The gold nanorod enhances fluorescence and the enhanced signal in the near-field of the gold nanorod was observed only in the presence of the far field (diffraction limited area) signal. (Vide supra).

The theoretical model of the correlation function was compared to experimental correlation functions. In the model of Langguth and Koenderink[?], the molecule detection function is considered as the superposition of two coinciding 2D Gaussians. We take a beam waist of 265 nm for the far field and 31 nm for the near-field. The total correlations

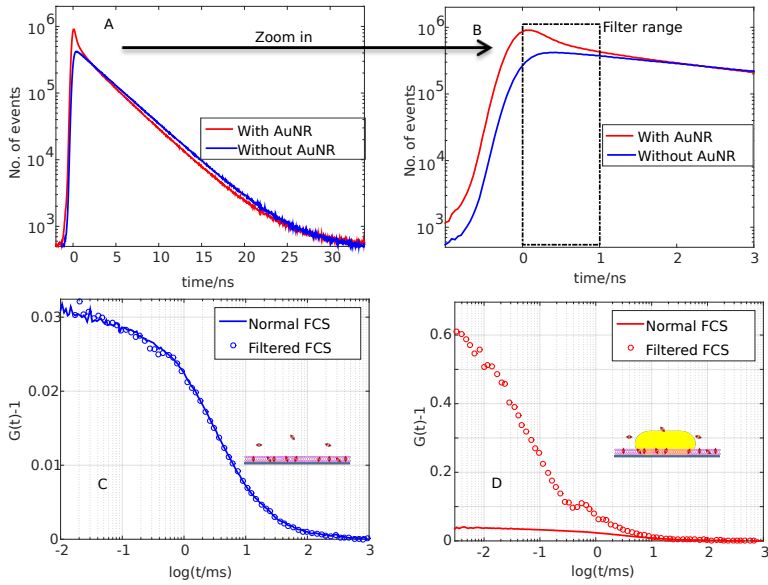


**Figure S1.13.** Filtering signal. (A) Fluorescence decay of 100 nM of ATTO 647N in the presence (blue) and absence (red) of a gold nanorod. (B) Zoomed-in part of the decay in Fig. S1.13A at shorter time scales. The dotted box indicates the range of arrival time of fluorescence counts considered for filtering the enhanced signal. The autocorrelation of normal and filtered time traces in absence (C) and presence (D) of nanorods. Notice the invariance of the correlation in the absence of nanorods and the significant improvement in the correlation contrast in presence of the nanorod.

were calculated as:

$$G(\tau) - 1 = \frac{1}{\langle C \rangle S_{MDF}^2} \left[ \sum_n A_{nn}(\tau) + \sum_{n \neq m} A_{nm}(\tau) \right], \quad (1.6)$$

with n, m = F (far-field), or N (near-field),

$$A_{n,m}(\tau) = S_n S_m \left[ \frac{2}{\pi ([\omega_n]^2 + [\omega_m^D(\tau)]^2)} \right], \quad (1.7)$$

$\omega_m^D(\tau) = \sqrt{\omega_m^2 + *D\tau}$ ,  $S_n = P_n \times A_n$  and  $S_{MDF}^2 = \left[ \sum_n S_n \right]^2$ , where  $P_n$  indicates the peak intensity and  $A_n$  the area of the Gaussian distribution. Figure S1.12C-D shows calculated correlations for different peak intensity ratio ( $P_F/P_N$ ). The red curved indicates the total correlation function and the other curves represent individual correlations (blue, green and magenta) that contribute to the total correlation. Here we would like to emphasize that the contribution of the cross terms (AFN) between far-field and near-field is not negligible, especially at low peak intensity ratios.

**Lifetime-based selection** Correlation for shorter lifetime photons (enhanced signal) was obtained using only the photons arriving within 1 ns after the excitation pulse. The

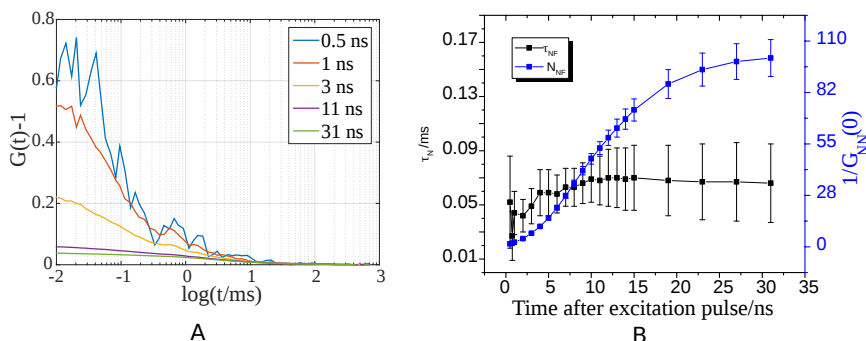


**Figure S1.14.** Effect of cut-off range. (A) Autocorrelation of time trace of ATTO 647N after lifetime filtering. The corresponding times after the excitation pulse are shown in the legend. Notice the significant increase in the noisiness between filtering times 1 ns (red) and 0.5 ns (blue). (B) Effect of the selection time window on the near-field correlation parameters. The near-field diffusion time is shown in black indicating minimal changes of time with selection range, whereas the number of molecules in the near field, shown in blue, undergoes a significant reduction.

blue decay in Figure S1.13A represents the fluorescence decay of ATTO647N in the absence of gold nanorods and the red one in the presence of the gold nanorod. It can be clearly seen that the lifetime histogram in presence of the nanorod exhibits a multicomponent decay. All the photons falling in the dotted box in Figure S1.13B were selected for correlation. While the FCS curve in the absence of the nanorod remained unchanged as can be seen in Figure S1.13C, the FCS contrast within the presence of gold nanorods showed a significant improvement. This is because of the selective consideration of the enhanced signal in the near field and suppression of background coming from far field.

### Effect of cut-off range

**Fluorescence enhancement in 3D diffusion** Fluorescence enhancement experiments were performed with 10 nM ATTO 647N in 70 % sucrose solution and gold nanorods on glass substrate. We observed an average intensity of 50 kcps observed for five molecules in the diffraction-limited volume in the absence of gold nanorods. The intensity from a single molecule was 10 kcps. In presence of gold nanorods, bursts with a maximum of 1200 kcps were observed corresponding with an enhancement factor of 110. (Figure S1.14)

The enhancement factor of 110 is far bigger than the factor of 4 observed in the case of the lipid bilayer. The lifetime remained the same both in the bilayer and in the sucrose solution indicating no change in the quantum yield. The difference in the enhancement factor can be explained by the accessibility of the hot spot for the diffusing molecules. The nanorod used in the experiment is 50 nm thick. In case of a bilayer, we suppose that the molecules are confined at the bottom to a layer of 5 nm thick. Hence the diffusing molecules are not able to explore the most intense region of the hot spot, resulting in a weaker enhancement. In the case of sucrose, however, the dye molecules diffuse through

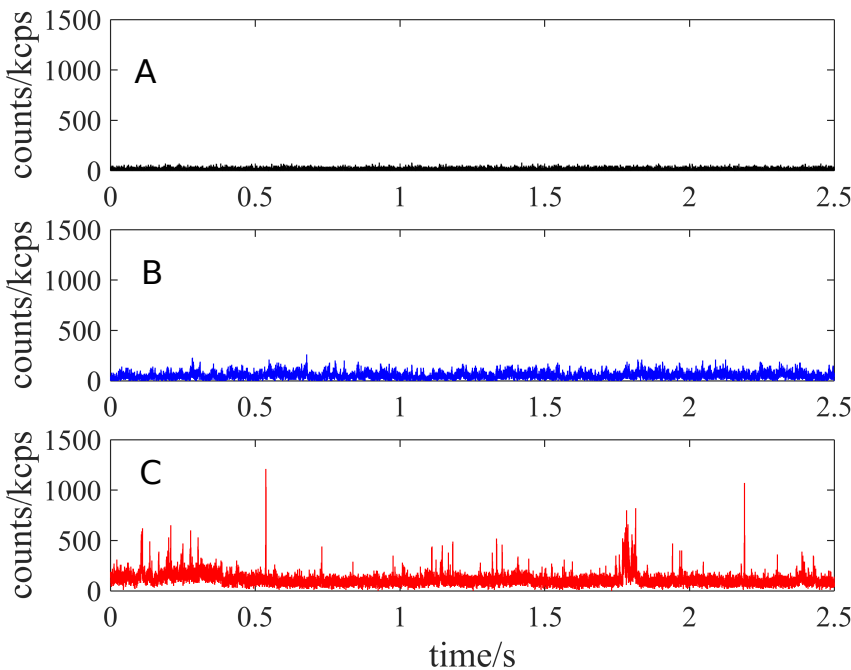


**Figure S1.15.** Time traces with a binning time of  $100\mu\text{s}$  of (A) Gold nanorod in sucrose with a constant intensity of  $20\text{kcps}$ ; (B) ATTO647N without gold nanorod in sucrose with average intensity of  $SI51\text{kcps}$  for 5 molecules on average, as obtained from the autocorrelation function. This translates into a brightness of  $10\text{ kcps/molecule}$ ; (C) ATTO 647N with gold nanorod in sucrose with a maximum intensity of  $SI1200\text{ kcps}$ . Hence the fluorescence of ATTO 647N was enhanced by a factor of 110 by the gold nanorod.

1

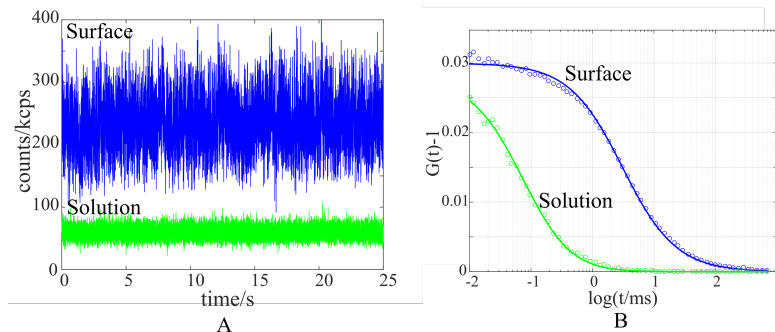


**Figure S1.16.** A) Time traces with a binning time of 1 ms of ATTO 647N on surface (blue) with an average intensity of 235 kcps and in solution (green) with an average intensity of 60 kcps. B) Autocorrelation of time traces of ATTO647N on surface (blue) and solution (green). Notice the absence of correlation component corresponding to the solution in the blue curve. The high background from the surface suppresses the correlation contrast of the dye in solution. The similar magnitude of the autocorrelation contrasts indicates that the number of molecules on the surface is almost the same as the number of molecules in the three-dimensional detection volume in solution. As the dye has a certain partition coefficient between the surface of the bilayer and the solution, the dye content on the surface can be controlled simply by changing the dye concentration in the solution.

the whole space around the nanorod and occasionally reach the intense hot spot region resulting in a larger maximum fluorescence enhancements. This observation confirms the assumption that the bilayer does not cover the tips of the rod.

#### Partitioning of the dye between surface and solution

# 2

## DYNAMIC HETEROGENEITY IN SINGLE ELECTRON-TRANSFER-PROTEINS

### INTRODUCTION

Introduction here.

### EXPERIMENTAL SECTION

**Protein synthesis.** Azurin (wild type) from *Pseudomonas aeruginosa* was expressed in *E. Coli* and purified as described before [43]. BL21 *E.coli* cells were transformed with PGK22 plasmid that carries the gene for azurin. The cells were cultured in Luria Bertani (LB) medium. Then the cells were harvested and resuspended in a 20 % (w/v) sucrose solution in Tris pH 8 buffer containing 1 mM EDTA. The solution was centrifuged (8000 rpm, 20 min) and the supernatant was collected. Copper sulfate was added to the solution for insertion into the active site of azurin. The unwanted proteins were precipitated by addition of concentrated acetic acid until pH 4. The turbid solution was centrifuged at 8000 rpm for 20 min. The supernatant was loaded on a CM Sepharose fast flow column and elution was performed in an Akta purifier (GE Healthcare) with a pH gradient from 4 to 6.9 in 50 mM ammonium acetate. Fractions containing azurin (inferred from the absorbance at 290 nm and 620 nm) were collected and reduced with sodium dithionite. At this moment the solution contained both zinc and copper azurin. The azurins were purified in a DEAE sepharose column by a salt gradient of 0 to 50 mM NaCl in Tris pH8 buffer. Fractions containing copper azurin and zinc azurin were collected and concentrated separately. The purity of the samples was checked by sodium dodecyl sulphate (SDS)-polyacrylamide gel electrophoresis (PAGE) and UV/Vis spectroscopy (Cary 50 spectrophotometer, Varian Inc., Agilent Technologies, USA). The azurins appeared on SDS gel page at ~14 kDa. Both zinc and copper azurin showed a characteristic shoul-

der at ~290 nm while Cu azurin showed an additional broad absorption peak at 620 nm when oxidized as can be seen in Figure S2.8. The ratio  $O.D_{628\text{nm}} / O.D_{280\text{nm}}$  for Cu azurin was 0.56 which indicated that all the azurin molecules had a Cu atom. The concentrated protein was stored at 80 °C until further use.

## 2

**Fluorescent labeling.** The labeling protocol was based on previous work [44]. ATTO655 NHS-ester was bought from ATTO-TEC GmbH and used without further purification. The azurin solution was equilibrated with HEPES pH 8.3 for higher efficiency of amine-NHSester reaction. ATTO655 was chosen to label the protein because of its photostability and inertness (unreactive) to the redox chemicals used in the study. A mixture of 200 μM azurin and ATTO 655 NHS-ester (1:1) was incubated for 45 min. The NHS-ester group reacts with one of the amine groups on the protein. The unreacted dyes were removed with a HiTrap desalting column. The labeled protein was concentrated in Tris pH 8.5 buffer by centrifuging in a 3 kDa Amicon ultra filter. The labeled protein was further purified by an ion exchange chromatography in a 1 ml MonoQ column (GE Health). The different peaks obtained (see Figure S2.7) correspond to different numbers and positions of the dye on the azurin surface. The peak-III corresponds to the protein labeled at Lysine122 position [44]. For this position of the dye, the protein construct shows a high fluorescence switching 90 % ratio between oxidized and reduced condition as can be seen in Figure S2.7. This fraction was chosen for our single-molecule experiment as the two states can be observed easily. The same protocol was used for Zn azurin labeling and similar peak separations were observed. The fluorescently labeled proteins were then reacted with biotin-PEG-NHS (MW 3400) in phosphate-buffered saline (PBS) pH 7.4 buffer with a ratio 1:5 to make sure each protein has at least one biotin. The free biotin was then removed by centrifuging in a 3 kDa Amicon ultra filter. The biotin on the protein will be used for immobilization on the glass surface.

**Functionalization of cover slips.** The functionalization of glass surface was achieved according to previous work with a little modification.[45] Glass coverslips (Menzel-Glaser, 22 mm×40 mm, no. 1 thickness) were used for immobilization. The cover slips were sonicated in water (15 min) and acetone (15 min). Then they were rinsed in Milli-Q water several times and incubated in a  $\text{H}_2\text{O}/\text{NH}_4\text{OH}/(\text{H}_2\text{O}_2)$ (5:1:1) bath at 70 °C for removing organic impurities on the surface. The coverslips were rinsed several times with water and ethanol and finally stored in ethanol. Before functionalization, the slides were flamed and treated for 30 min with a 1 % solution of [3-(2-aminoethyl)aminopropyl]trimethoxysilane in methanol containing 5 % glacial acetic acid. This results in the binding of the silane to active hydroxyl groups. At this stage the silane is not yet covalently bound, but this is achieved by baking the cover slips in an oven at 65 °C for 3 h. After this treatment, the cover slips were sonicated for 10 min and washed with methanol. Dried with clean nitrogen, they were left in a desiccator overnight. The next day they were treated with a mixture of 5 mg ml<sup>-1</sup> methoxy-PEG-N-hydroxysuccinimide (MW 2000, Laysan Bio) and 0.05 mg ml<sup>-1</sup> biotin-peg-N-hydroxysuccinimide (MW 3400, Laysan Bio) in 50 mM phosphate buffered saline (PBS), pH 7.4. This creates a surface containing biotin and methoxy end groups. The PEG surface prevents nonspecific adsorption of the protein. The slides were dried with a gentle flow of nitrogen and stored in a desiccator until further use.

**Protein immobilization.** The biotin functionalized glass slide was incubated with 20 mM PBS pH 7.4 buffer for 5 min. 100 nM of NeutrAvidin (Thermo Scientific) was incubated for another 15 min and then washed to remove unbound Neutravidin. Then 100 pM of the labeled protein was incubated for 1 min to get isolated proteins (20 per 100  $\mu\text{m}$  area) to bind to the functionalized glass surface. The unbound proteins were then removed by washing with fresh PBS buffer.

**Electrochemical-potential control.** Once the unbound proteins were removed, a new mixture containing 0.1 mM sodium ascorbate ( $\text{C}_6\text{H}_7\text{O}_6-\text{Na}^+$ ) and 0.2 mM potassium ferricyanide ( $[\text{Fe}(\text{CN})_6]^{3-}$ ) in 4 ml PBS pH 7.4 was added to the sample. The redox potential of the solution was further controlled by a potentiostat (Model 800B Series Electrochemical Detector, CH Instruments) with the same electrochemical set up as previously described[46] with little modification. A platinum rectangular grid (the total length/width of the grid is around 2.5 cm) was used as working electrode and pressed onto the sample slide with the help of a small glass slide. Not only is the pressure evenly applied on the grid, but also small confined volumes are formed where the sample slide and glass slide form the 'floor' and 'roof' and the platinum grid forms the 'walls'. These confined volumes are in the order of nanoliters, which makes switching of the electrochemical potential of the solution possible in a matter of minutes. The change in the solution potential changes the concentration of reductant and oxidant based on the Nernst equation.

**Confocal Microscope.** Single-molecule measurements were carried out in a home-built confocal microscope. The setup was equipped with a 635 nm pulsed diode laser (Power Technology, Little Rock, AR, USA) controlled by a PDL 828 "Sepia II" (PicoQuant) at 40 MHz repetition rate. The laser beam was passed through a narrow-band cleanup filter (Semrock LD01-640/8-25) and coupled to a single-mode optical fiber to obtain a Gaussian beam profile. The output beam was collimated and reflected by a polychroic mirror (z488/633rpc) onto the back aperture of an oil immersion objective (NA=1.4, Olympus UPLSApo 100x). The sample holder with the glass slide and electrodes was mounted on a scanning stage (Physik Instrumente P-517.3CD) controlled by a nanopositioning system (Physik Instrumente E-710.3CD). The epifluorescence light was collected back through the same objective and focussed on a 50  $\mu\text{m}$  pinhole for spatial filtering, then the light passed through an emission filter (z488/635m "dual"-band emission filter, Chroma). The fluorescence beam was re-collimated and focussed on a single-photon avalanche photo diode (SPCM AQRH-15, Perkin Elmer Inc., USA). The signal from the photo diode was recorded by a PicoHarp 300 (PicoQuant GmbH, Berlin, Germany) in time-tagged-time-resolved mode.

**Data recording.** A 20  $\mu\text{m} \times 20 \mu\text{m}$  area of the sample surface functionalized with sparsely distributed ATTO655-labeled azurin was scanned with 50 nm per pixel and with a dwell time of 1 ms per pixel. A typical fluorescence intensity image can be seen in Figure 2.1. A constant potential of 200 mV vs SCE (oxidizing) was applied by the potentiostat and an image of 10  $\mu\text{m} \times 10 \mu\text{m}$  area was taken after 2 min. Typically within one minute, the solution potential of the mixture of 0.1 mM ascorbate and 0.2 mM ferricyanide reaches

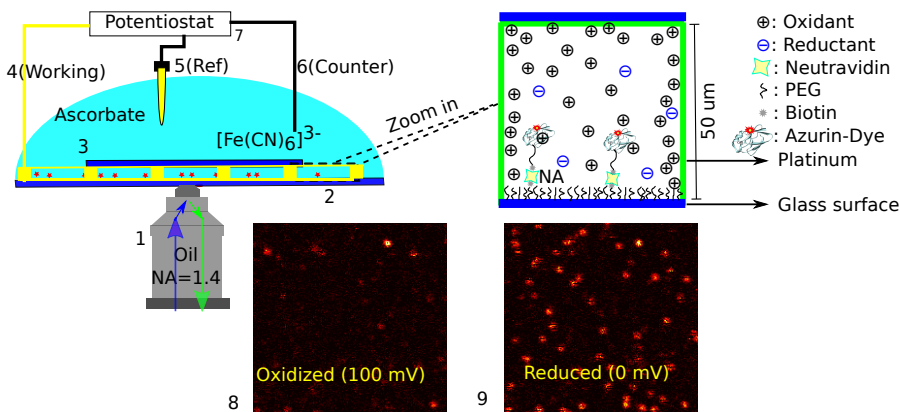


**Figure 2.1.** Schematic of the confocal and electrochemical setup. (1) Objective through which light is irradiated on and collected from the sample. (2) Functionalized sample slide with on top the platinum grid another small glass slide to press the grid on the sample slide, resulting in small confined volumes in the order of nanoliters. (3) Electron mediator solution containing  $200 \mu\text{M}$  ferricyanide,  $100 \mu\text{M}$  ascorbate in PBS (pH 7.4) buffer with a total volume of 4 mL. (4) Working electrode (platinum wire) that is in contact with the platinum grid (yellow blocks) with a height of 50  $\mu\text{m}$ . (5) Saturated calomel reference electrode. (6) The platinum wire (not touching the grid) as counter electrode. (7) Potentiostat (Model 800B Series Electrochemical Detector, CH Instruments) to which the electrodes are connected. Zoom-in picture shows the functionalization method and the working electrode around it. (8, 9) Confocal scanning images of the surface of the substrate at 100 mV (Oxidizing) and 0 mV (Reducing).

the applied potential. Another image of this same area was recorded at 0 mV (reducing). The two images were compared to identify the molecules that switch on and off at the two potentials (Figure-2.1 (8 & 9)). The coordinates of the switching molecules were registered and an automatic recording was started. For each molecule, time traces were recorded for 30 s at different potentials between -100 mV and +100 mV. To observe the dynamics of a single-molecule over longer period, time traces were recorded until the dye was bleached or the protein was denatured. Zn-azurin-ATTO655 was used as a control since it doesn't show switching at the above potentials. Time traces at the same potentials for the same durations were recorded as for the Cu-azurin.

**Data analysis.** The measurements resulted in more than a 1000 time traces. Each time trace contains the absolute arrival times of photons as well as the arrival time with respect to the excitation laser pulse. This enabled us to extract maximum information from the traces. To minimize accidental variation and improve efficiency, codes were written (in Python and Matlab) to standardize the analysis of the time traces. Each trace was analyzed in three ways (i) Intensity change points in the time traces were obtained using the Change-Point algorithm[47] provided by prof. Haw Yang (Princeton University, USA). This method is bin free and doesn't require any prior knowledge of the underlying kinetics. It determines the location of intensity changes based on the photon arrival times and the algorithm is recursively applied over the whole time trace to find all the changes. A Bayesian information criterion is used to find the number of states. In the present case two states were identified from long time traces of many molecules (2500 changepoints each) with more than 90 % accuracy. This was in agreement with our prediction of two states namely a FRET quenched (low intensity) and a non-quenched state (bright). Consequently the number of states for the other time traces have been set to two to minimize the computation time. An example of a trace with change points and its overlap with the real time trace can be seen in Figure-2.2. (ii) Autocorrelation of the time traces were calculated using SymPhoTime(PicoQuant) software. (iii) Further analysis of Change-Point outputs and the autocorrelation outputs were performed in Python.

## RESULTS AND DISCUSSION

**Time traces at different potentials.** Active Cu-azurin molecules were identified from their fluorescence intensity images at the oxidizing (200 mV) and reducing conditions(0 mV). In reducing conditions, the image contains many bright spots corresponding to Cu(I)-azurin-ATTO655 and more than 90 % of the molecules are turned off in oxidizing conditions (Figure-2.1(8)). The azurins on each sample slide showed active switching during the course of the experiment (up to two days) without any noticeable degradation. A set of active azurins were marked for recording and time traces at different potentials (between 100 mV and 100 mV) were measured on the same molecules for 30 s. Many of the labeled proteins bleached within the recording at a few potentials, but more than 50 % of the labeled-azurin survived at least five measurements (150 s total) at different potentials. Longer measurements were possible thanks to the scavenging of oxygen in the solution. Before recording the time trace, the solution was exposed to a negative potential for at least 1 h. Ascorbate is known to scavenge oxygen[48] and get oxidized.

2

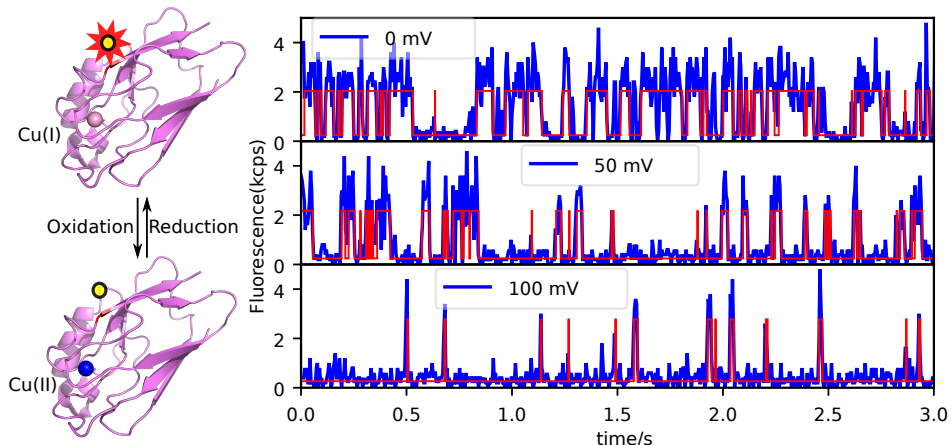


**Figure 2.2.** Time traces of the same Cu-azurin-ATTO655 at different potentials (0, 50 and 100 mV with respect to SCE). The structure of the protein with properly positioned dye can be seen in the schematic picture in the left. In the Cu(II) state (shown as blue dot in the protein structure), the dye is non fluorescent because of FRET and in the Cu(I) state (shown as a gray dot), the dye is fluorescent. Notice the amount of time the protein spends in the bright and the dark state at different potentials. At lower potentials (e.g 0 mV) the protein is bright most of the time because of the higher concentration of reductant.

The oxidized ascorbate is then reduced by the electrode and is again available to scavenge other oxygen molecules. In addition to the absence of oxygen, the oxidizing-and-reducing-system(ROXS) mechanism was also at play.[49] The reduction and oxidation of Cu-azurin made the dye switch on and off, hence the fluorescent dye spent less time in the bright state, and thus was less prone to bleaching. We could measure some fluorescence time traces for more than 1000 s.

Figure 2.2 shows time traces of a single Cu-azurin-ATTO655 molecule at three different potentials. The intensity changes from bright to dark and vice versa over time (Figure 2.2). The dark state is due to FRET from the dye to the Cu(II) absorption center[50]. Bulk (ensemble) measurements of the fluorescence intensity at completely oxidizing and completely reducing condition shows 90 % switching ratio (Figure S2.8) for the lysine-122 labeled Cu-azurin-ATTO655.[44] In the single-molecule traces in Figure 2.2, the quenched state is same as the background signal in absence of the protein. A measurement (Figure S2.10) at a higher laser power( $0.7 \mu\text{W}$ ) show that single azurin too show 90 % switching in their fluorescence, which is consistent with the bulk measurements. The intensity of the Cu(II)-state is lower than the intensity of the Cu(I)-state, but higher than the background (bleached state). Also the Cu(II)-state has a shorter lifetime (0.3 ns) than the Cu(I)-state (1.9 ns), but longer than the instrument response function (0.2 ns). Both intensity and life time confirm that the dim state is FRET-quenched. The high FRET efficiency is due to the small distance of the dye to the absorption center. This clear distinction between the on and off state was very important for the low laser power and lower signal mea-

surements. At higher potential (100 mV), the protein spends most of its time in its dark state and as the potential is lowered, the molecule spends more and more time in bright state. This longer on-times at lower potentials is due to the increase in the concentration of the reductant species in the solution. A control study with Zn-azurin-ATTO655 (Figure S2.9 and Figure S2.11) shows that the dye itself blinks below 40 mV. Zn-azurin is inert to redox changes and thus the blinking can only originate from the interaction of the dye with the reductant through photo excited electron transfer. To simplify the analysis, therefore only potentials above 40 mV were considered for the Cu-azurin-ATTO655 study.

**Midpoint potential of single azurins.** Figure 2.3a shows the ratio between the average off-time ( $\bar{t}_{off}$ ) and average on-time( $\bar{t}_{on}$ ) plotted against the applied potential. The relationship of this ratio with the potential is given by the Nernst equation:

$$E = E_0 - \frac{k_B T}{ne} \ln\left(\frac{\bar{t}_{on}}{\bar{t}_{off}}\right) \quad (2.1)$$

where  $E$  is the applied potential,  $E_0$  the midpoint potential,  $k_B$  the Boltzmann constant,  $T$  the absolute temperature,  $n$  the number of electrons involved in the reaction and  $e$  the electron charge. The value of  $n$  was found to be 1 from the data analysis when the slope in the Nernst equation is kept as a free parameter (see Figure-S2.12). Each color represents a single-azurin and the solid line connecting the points is the fit with the Nernst equation. Labeled proteins surviving at least three potentials above 40 mV were used for the fit. The potential at which the off-on ratio equals 1 is the midpoint potential. The distribution of midpoint potentials (Figure 2.3b) from 132 molecules can be fitted by a Gaussian with a center value of  $\langle E_0^{SM} \rangle = 4.5 \pm 1.2$  mV and a full width half maximum (fwhm) of  $\sigma^{SM} = 36 \pm 3$  mV. The midpoint potentials are similar to previously reported values of  $6 \pm 0.6$  mV with  $fwhm = 150$  mV where each  $E_0$  was calculated from a cluster of about 1000 molecules.<sup>[51]</sup> Another work reported  $E_0 = 16$  mV with low surface coverage (100 s of azurins) with a fwhm of 70 mV.<sup>[52]</sup> Recently, for truly single azurin, a midpoint potential of  $E_0 = 12 \pm 3$  was reported with fwhm of 92 mV.<sup>[53]</sup>

The small width of the distribution (36 mV) of single-azurin midpoint potentials in this work is obtained probably because of the way the proteins are functionalized to the surface. The azurin is attached to a PEG-chain with a length of ~20 nm. The PEG chain is attached to the surface through NeutrAvidin. Such functionalization minimizes the interaction of the protein with the surface. Indeed, no proteins were bound to the surface if the Neutravidin is taken out showing the non-sticking nature of the protein. In previous experiments, the azurin was either non-specifically attached to the surface or attached through a very short linker (<1 nm). Surface interactions with different hydrophobic and charged patches on the protein can alter the ET functionality of the enzyme.

**Intermediate detection from on-off histogram.** The number of on-off events for a single azurin was limited by fluoresce bleaching and led to noisy distribution. For this reason we first analyzed the overall distribution of on- and off-times of all the single

2

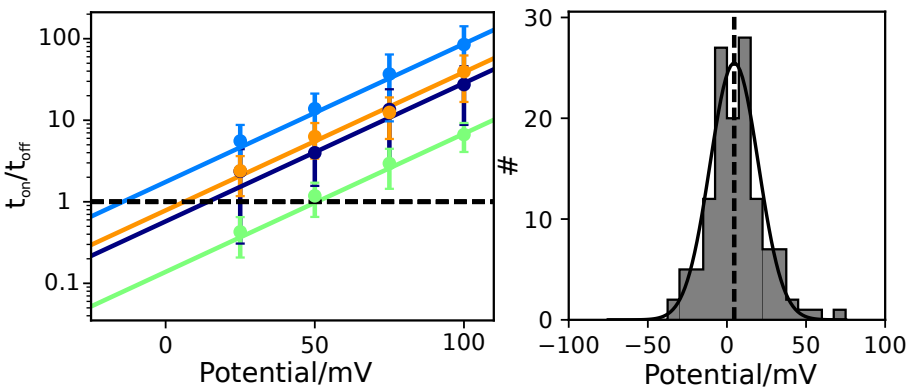


**Figure 2.3.** Ratio between on and off times as a function of applied potential for the same single azurin. Different colors represent different single molecules. The line connecting the data points is the Nernst fit with  $n = 1$  for all the data points above 40 mV. The plot at the right is the histogram of midpoint potentials for 132 molecules with a Gaussian fit with a center value of 4.5 mV with respect to calomel electrode.

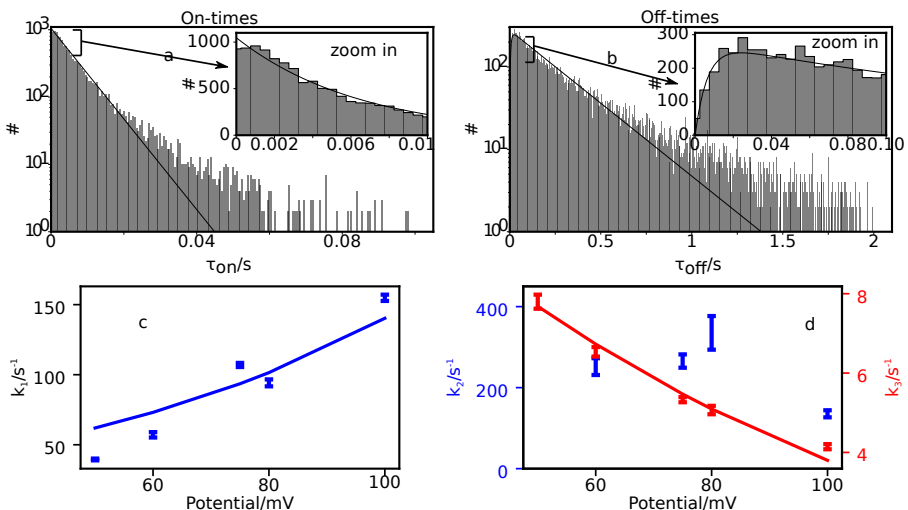
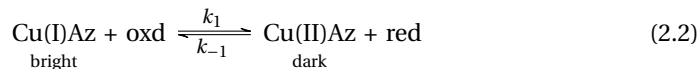
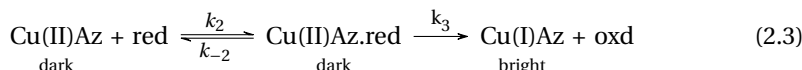


**Figure 2.4. Electron transfer rates (many molecules)** The histogram of on-times (a) and off-times (b) obtained from 132 single-Cu-azurin-ATTO655 molecules at 100 mV with their zoomed in part in the inset. Notice the single exponential decay of on-times and the bi-exponential (with rise time) for the off-times. This indicates that reduction of Cu-azurin occurs through an intermediate step while for oxidation the intermediate state is not observable. The solid line is the corresponding single-exponential fit to the distribution. (c) The rate constant for oxidation as a function of the potential. (d) The rate constant for reduction as a function of redox potential: blue points correspond to the faster rate constant (rise,  $k_2$ ) while the red points represent the slow rate constant ( $k_3$ ).

molecules obtained at a certain potential which basically can be considered as ensemble measurement. Figure 2.4(a) shows the histogram of on-times at 100 mV and the solid line is the fit of a single exponential with a time constant ( $k_1$ ) of  $155\text{ s}^{-1}$ . The on-time represents the time the protein spends in the reduced state before getting oxidized according to the following reaction scheme:



In contrast, the distribution of off-times shows a non-exponential distribution with a rise time (Figure 2.4(a)). The inset with binning time 5 ms clearly shows that the probability of finding very short off-times is relatively small. This distribution can be explained with the Michaelis-Menten mechanism:



where  $k_2$  is the pseudo-first order rate constant which depends on the concentration of reductant and  $k_3$  is the zero order rate constant which should be independent of the concentration of the substrate. When assuming  $k_{-2} = 0$ , the probability distribution of off times is given by[54]

$$P(t_{off}) = \frac{k_2 k_3}{k_3 - k_2} [\exp(-k_2 t_{off}) - \exp(-k_3 t_{off})] \quad (2.4)$$

At 100 mV,  $k_2$  for the reduction is  $4.1\text{ s}^{-1}$  while  $k_3$  is  $135\text{ s}^{-1}$ . The data doesn't match with a single component distribution which is not surprising as the distribution is built from many single azurins and each azurin has its own decay. Similar to the distribution in midpoint potential, the non-exponential distribution is a reflection of the statistical heterogeneity among the azurins.

The rates were determined at different applied potentials. As expected the rate constant for the intermediate complex formation ( $k_3$ ) is dependent on the substrate concentration thereby the potential while the rate constant for electron transfer in the intermediate is independent of the potential (Figure 2.4(c)). The rate of complex formation can be modeled as:

$$k_3 = k_3^0 \times [R] \text{ and } k_1 = k_1^0 \times [Ox] \quad (2.5)$$

$$[R] = \frac{R_0 \exp(\frac{E_0^R - E}{0.059})}{1 + \exp(\frac{E_0^R - E}{0.059})} \text{ and } [O] = \frac{O_0}{1 + \exp(\frac{E_0^O - E}{0.059})} \quad (2.6)$$

$[R]$  is the concentration of reductant (equivalent to "substrate" in enzymology),  $R_0$  is the starting concentration of reductant in the potentiometry which is equal to the concentration of Ascorbate in this case,  $E_0^R$  is the standard redox potential of Ascorbate that is 30 mV and  $E$  is the applied potential. The value 0.059 stands for  $\frac{RT}{nF}$  similar to the slope in the Nernst equation(Eq. 2.1) with  $n = 1$ . Similarly  $[O]$  represents the concentration of the oxidant (Ferricyanide) at different applied potential. The maximum rate constant of reduction ( $k_3^0$ ) was obtained to be  $3.3 \times 10^5\text{ M}^{-1}\text{s}^{-1}$  while the maximum rate constant oxidation was  $1.3 \times 10^8\text{ M}^{-1}\text{s}^{-1}$ .

**Dynamical heterogeneity.** After looking at ~150 single-azurins together in an ensemble fashion, we investigated single azurins for as long time as their fluorescence survived. Figure 2.5 shows the statistics of a single-azurin at 100 mV that survived for ~350 s. Zoom-in of two different parts of the original time trace are shown in Figure 2.5A and B with the respective part color-shaded in the trace Figure in 2.5C. The two zoom-in traces have very different on-off characteristics, the one on the left has short on-times and long off-times while the one on the right has long on-times and short off-times. The time trace was divided into small parts and the average was calculated over every 10 consecutive on- and off-times (Figure 2.5E,G). The averaging was done to smooth out the noise and to show few number of points on the whole trace which makes it easy to observe the difference. Unlike random (Gaussian) noise, spikes and correlated high-low events are observed on the on-and off-trace which is also reflected in the density of points per unit time, longer on and off-times resulting lower density of points. The histogram of on- and off-times are shown on the left side of the on-off-trace without any averaging and the fit is shown with a single exponential function. The distribution is clearly non-exponential as can be seen from the big deviation from an exponential fit. The trace of midpoint potential (Figure 2.5I) is calculated from each point on the on-off-trace and the applied potential based on the Nernst equation. The midpoint potentials in the trace also fluctuates in a non-random way which can also be seen in its non-Gaussian distribution (Figure 2.5H) with an average value of 42.2 mV.

The heterogeneity in the on- and off-times is related to the heterogeneity in the rate of electron transfer particularly the longer on-off-times which is the rate of intermediate-complex formation. The first reason we should consider is the effect of surface. Previous study shows that the azurin can stick to the hydrophobic surface through the different hydrophobic patches on the protein surface.[52, 53, 55] However, special care was taken to keep the protein as separated as possible from the surface thorough non-interacting PEG-surface and through a long (~20 nm) linker. Indeed no azurin was found attached to the surface of the substrate when the labeled azurin was flown onto the surface without Neutravidin or Biotin (everything else in the functionalization method kept same) indicating the non-sticky nature of the surface. The narrow distribution (narrower than any measurement before) of midpoint potentials among the 132 single azurins (Figure 2.3) also indicates the absence of interaction with the surface. From these observations, the surface contribution to the heterogeneity can safely be ignored. Also the solution potential controlled by the potentiostat is very stable and the concentration of the reductant and oxidant can be considered non-changing and in steady state.

The heterogeneity in the rates can now only attributed to the changes in the conformation in the protein. These changes are much smaller( $<4\text{ kJ mol}^{-1}$ ) in comparison with the change in the free energy( $-23\text{ kJ mol}^{-1}$ ,  $\Delta G = -nEF$ ) related to the change in the oxidation state of azurin. Such small changes can be attributed subtle changes in the structure of the protein, each of these sub-structure are called conformational sub-states.

The protein remains in a certain conformational sub-states for a duration of time which can be observed in the time trace. A short on-time followed by short on-time represents one state while a long on-time followed by long on-time represents another sub-state. The residence time in each of these conformational sub-states can be char-

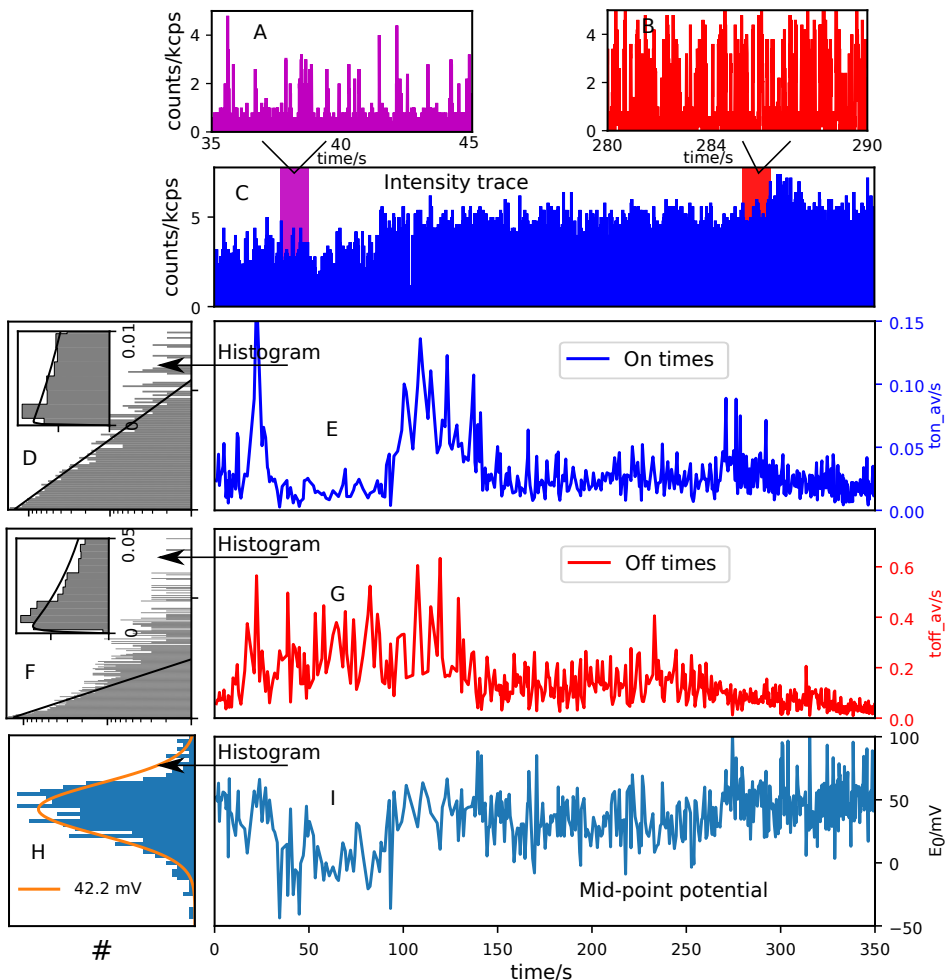


**Figure 2.5. Dynamic heterogeneity.** A long time trace (C) of Cu-azurin-ATTO655 at 100 mV with zoom-in (A, B) at different point of its time course. Variation of on-times(E) and off-times(G) of the same azurin is shown with their histogram on the left. The rates were averaged over every five consecutive rates to get rid off the noise and for easy visualization. The trace of midpoint potential(I) calculated from the on- and off-times and the the histogram(H) of midpoint potential is shown on its left with an average value of 42 mV.

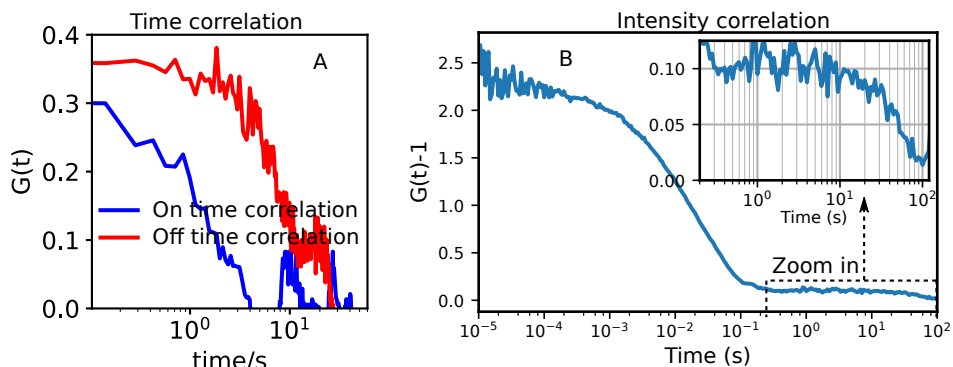


**Figure 2.6. Dynamic correlation.** (A) Autocorrelation of the on- and off-times in the trace showed in Figure 2.5E,  $G$ . (B) Autocorrelation of the intensity trace showed in Figure 2.5C. The inset shows the zoom-in of the intensity correlation in the longer time scale.

acterized by autocorrelating the time trace of on- and off-times (Figure 2.6 A). The characteristic decay times are in the order of 10s of seconds, however the decay time for on- and off-events are not the same. The signature of the changes in the rates can also be seen in the intensity correlation (Figure 2.6B) with a decay at round  $\sim 50$  s which basically has both the information about the on- and off-rates. However, the individual rates related to on- and off-time can't be extracted from the intensity correlation unless the underlying kinetics is known.

In 1980s, conformational sub-states were observed in the association and dissociation of carbon monoxide (CO) with myoglobin in bulk experiment where sub-populations were found with different binding rates of CO. The time scales of binding were stretched from microseconds to seconds indicating all possible conformations of myoglobin. Indication of heterogeneity has also been observed for single-enzymes with some success ( $\beta$ -galactosidase, flavoenzymes)[54, 56, 57]. Here the dynamic rates can be observed for single azurin in the time scale of 10s of seconds which varies from protein to protein as can be seen in SI Fig. S2.19 As the rate of oxidation and reduction occur in the range of 100s of milliseconds, conformational changes in the shorter times scale can't be determined. Among the proteins that were recorded, no two proteins seemed to have the same dynamics indicating the vast number of conformational sub-states that a protein can take. It was almost impossible to experimentally build a map of such a large number of states.

## CONCLUSION

The results presented here show how to controllably switch the solution potential and determine the switching ratio of redox active azurin. By introducing non-interacting surface and long linker, very narrow distribution in the midpoint potential obtained. The distribution over many single-azurin was found to be very close to the distribution of a single-azurin over long time. The rate of intermediate formation for the reduction process has been observed conferring to Michaelis-Menten mechanism. The intermediate

formation for the oxidation was too fast to be detected with our signal to noise ratio. In principle similar measurement at higher laser power and for many molecules should enable the detection of the intermediate if there is any. For the first time, correlated dynamics observed in the ET azurin. We showed several ways like non-exponential distribution rates of ET, non-Gaussian distribution of midpoint potentials, correlations of the rates of ET and correlation of intensities to characterize the dynamic-heterogeneity in the activity of the protein. Our study convincingly proves the presence of conformational heterogeneity in an enzyme and we expect to have similar heterogeneity in all types enzymes and electron transfer proteins in the nature.

## SUPPORTING INFO

**Fluorescence switching in bulk.** Fluorescence measurements in bulk of different peaks of azurin-ATTO655 sample (Figure S2.7) were carried out to determine the FRET switching ratio. The measurements were done in Cary Eclipse Spectrometer (Varian Inc. Agilent Technology, USA). A 50 nM sample was excited with 665 nm and intensity was monitored above 675 nm. Sodium ascorbate (reductant) and potassium ferricyanide (oxidant) were added alternatively. Among all the labeled position, peak-III showed maximum switching ratio and it's intensity change can be seen in Figure S2.8. Similarly Zn Azurin-ATTO655 showed little or no change in intensity.

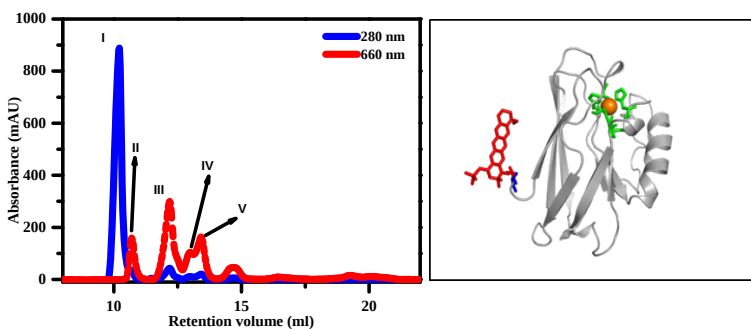


**Figure S2.7.** Peak separation: (a) Elution profile of Cu azurin sample after labeling and removal of free dye. 280 nm absorption that tells the presence of protein is shown in blue and 660 nm absorption that tells the presence of dye is shown in red. The protein structure with the dye at Lys corresponding to peak-III is shown in the right. A proper structure will be replaced

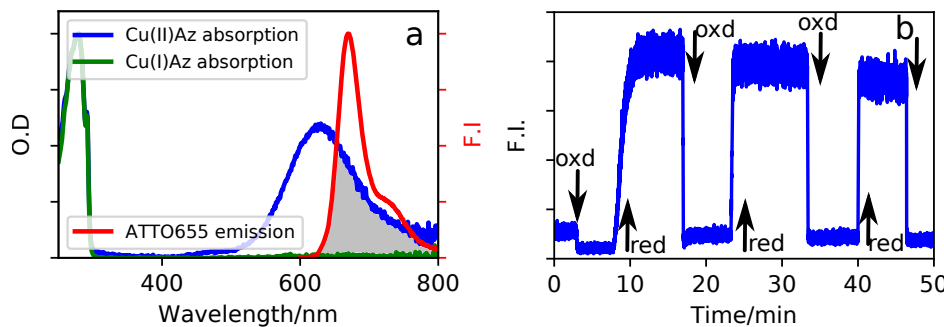


**Figure S2.8.** Spectral overlap and Bulk switching: (a) Absorption spectrum of Cu(II)azurin (blue), Cu(I)azurin (green). The emission spectrum of ATTO655 (red) has a good overlap with the absorption of Cu(II)azurin to show high FRET. (b) Fluorescence intensity of 50 nM CuAzurin-ATTO655 shows high intensity in the presence of reductant and low intensity with oxidant. The switching ratio comes to be 90 % satisfying the requirement for single-molecule FRET.

2

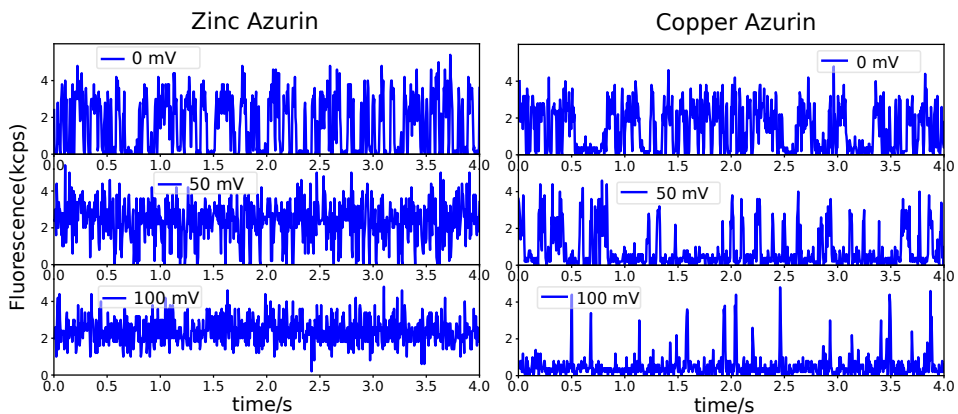


**Figure S2.9.** Time traces of Zn Azurin (left) and of Cu Azurin (right) labeled with ATTO655 at different potential. Above 40 mV, Cu-Azurin show switching in the intensity due to changes in the oxidation state of the Copper metal center and below 40 mV, triplet blinking contributes to the switching as can be seen in the redox inactive Zn-Azurin. To keep the analysis simple, time traces above 40 mV were chosen for Cu azurin

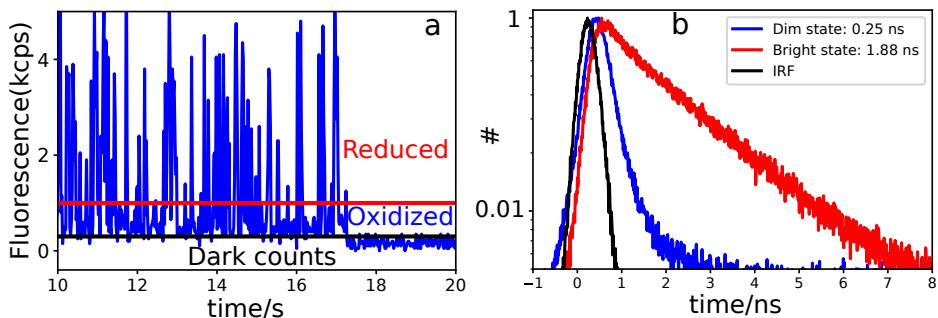


**Figure S2.10.** Single-molecule azurin switching and lifetime. (a) Time trace of a single Cu azurin at 50 mV with a binning time of 50 ms. Notice the three different labels indicated in the figure. Bright (Cu(I)) state as above the red line, oxidized state is between red and black and Dark counts are below the black line. The fact that the molecule doesn't go to the dark count label before being bleached shows that the transitions are due to Copper oxidation switching rather than triplet blinking of the dye. Once the fluorophore is bleached, no transitions were observable. (b) The lifetime histogram corresponding to bright state (red), oxidized state (blue) and instrument response function (black). The lifetime of oxidized state is much shorter than the reduced state due to FRET quenching.

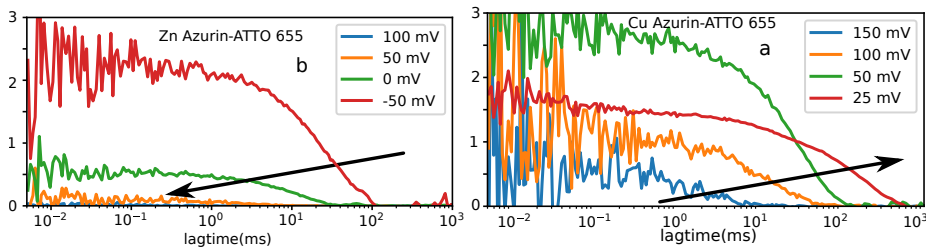


**Figure S2.11.** Autocorrelation of time traces of Cuazurin-ATTO655 (a) and Znazurin-ATTO655 at different potential. At lower potential, Cuazurin-ATTO655 has longer correlation time (on time) which shows that the molecule spends more time on the Cu(I) state. But below 50 mV the dye (ATTO655) starts to show triplet blinking. As potential is lowered the triplet blinking dominates. The Cu azurin study is focussed in the safe window of potential more than 40 mV where triplet blinking is absent.

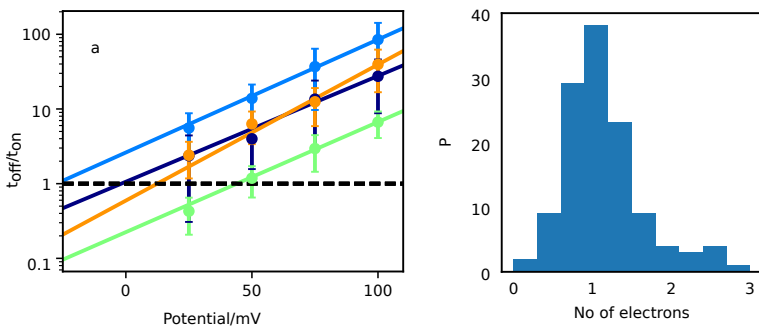


**Figure S2.12.** Fitting with Nernst equation with slope as variable parameters for (a) Cu-Azurin ATTO655. (b) The corresponding histogram of slopes obtained from the fitting shown in the left. The distribution of slope is centered around 59 mV indicating that Cuazurin switching involves only one electron.

2

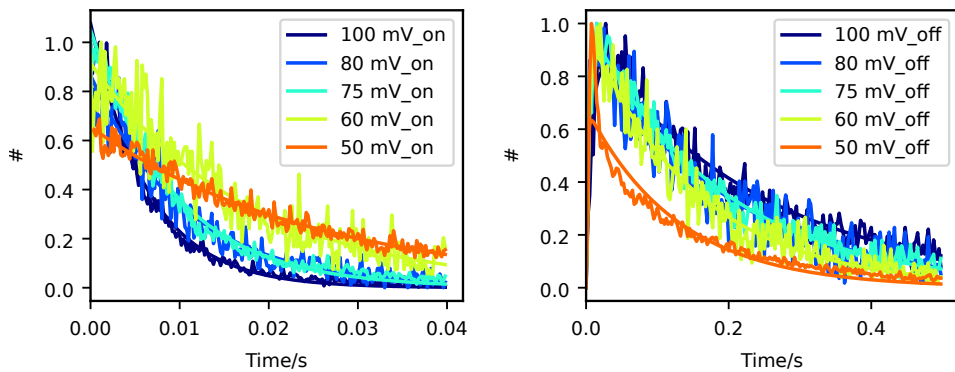


**Figure S2.13.** (a) Fitting of on time distribution with monoexponential at different potential. (a) Fitting of off time distribution with bi-exponential equation with rise time as shown in the main text at different potential. The output rate constants were plotted against potential (see main text)

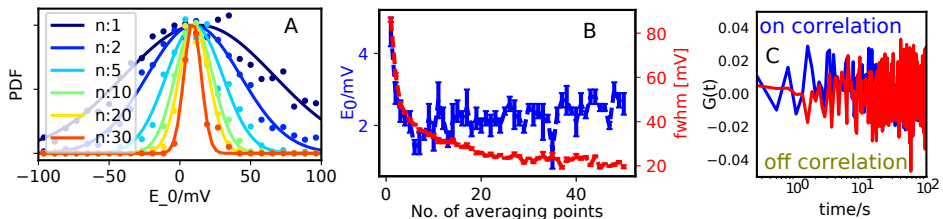


**Figure S2.14. No correlation dynamics.** Variation of midpoint potential and fwhm with the number of on and off times taken for averaging for the long trace shown in the main text (Figure-2.5). At around 20 events, both  $E_0$  and fwhm reaches plateau. The averaging of on-time and off-times for correlation and midpoint distribution were done every 20 events.

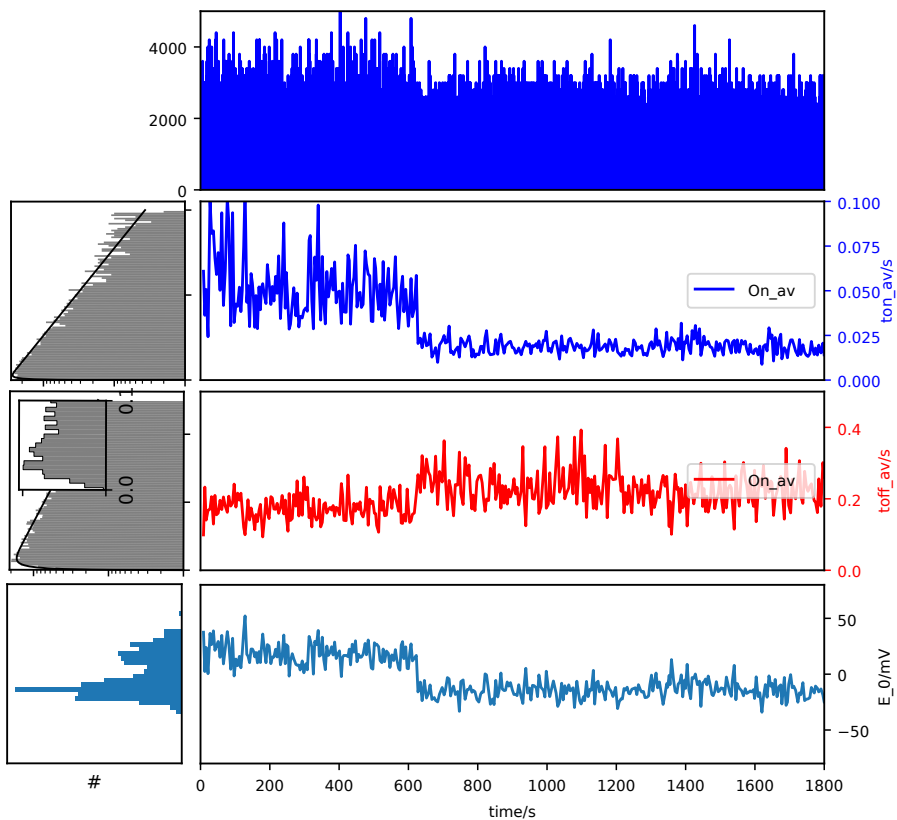


**Figure 2.15.** Two conformational state dynamics

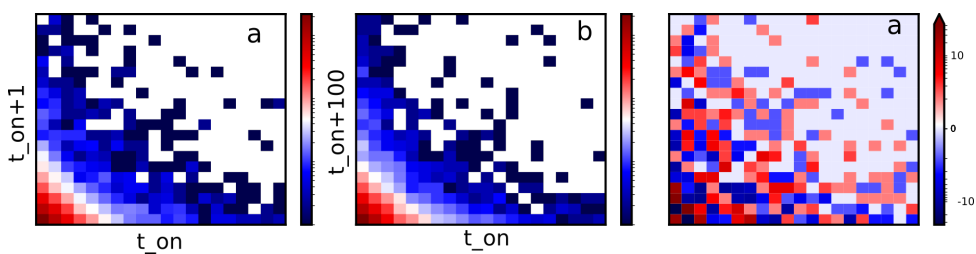


**Figure 2.16.** **2D histogram: Cu-Azurin.** Two-dimensional correlation plot of a single azurin at 50 mV of (a) adjacent waiting time for oxidation ( $t_n$  and  $t_{n+1}$ ) (b) two waiting times at a large separation of 100 ( $t_n$  and  $t_{n+100}$ ) (c) The difference two dimensional histogram of (a) and (b).

2

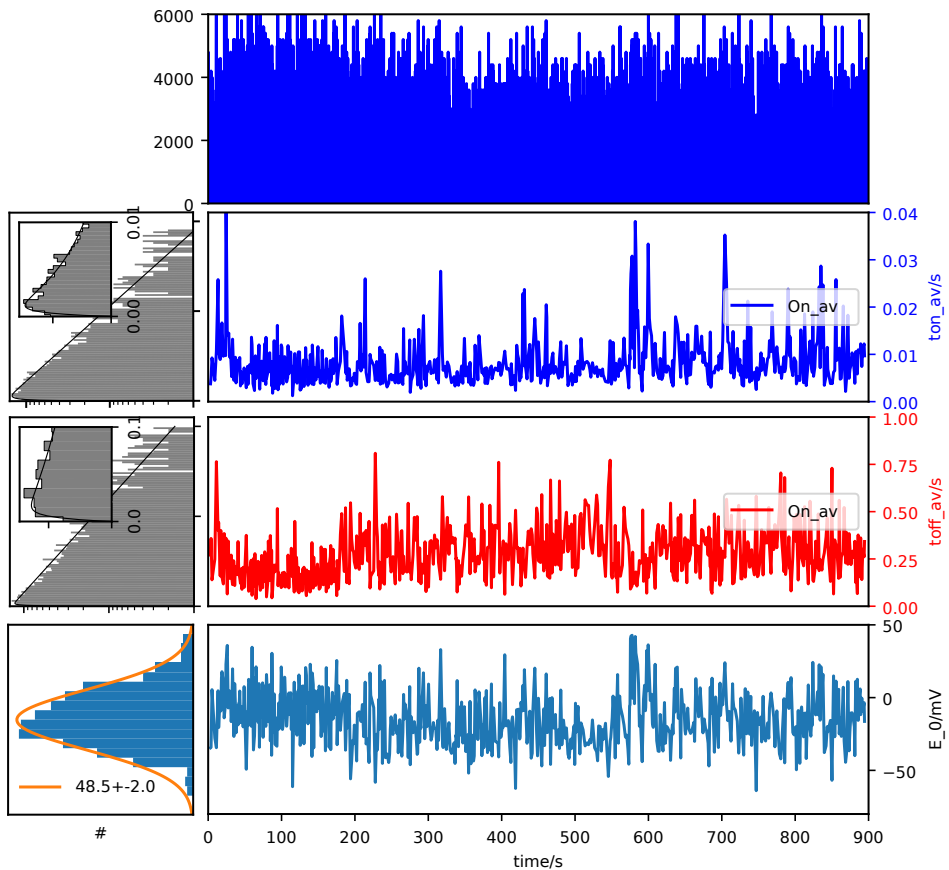


**Figure 2.17. dynamic Point 20 75mVS105**

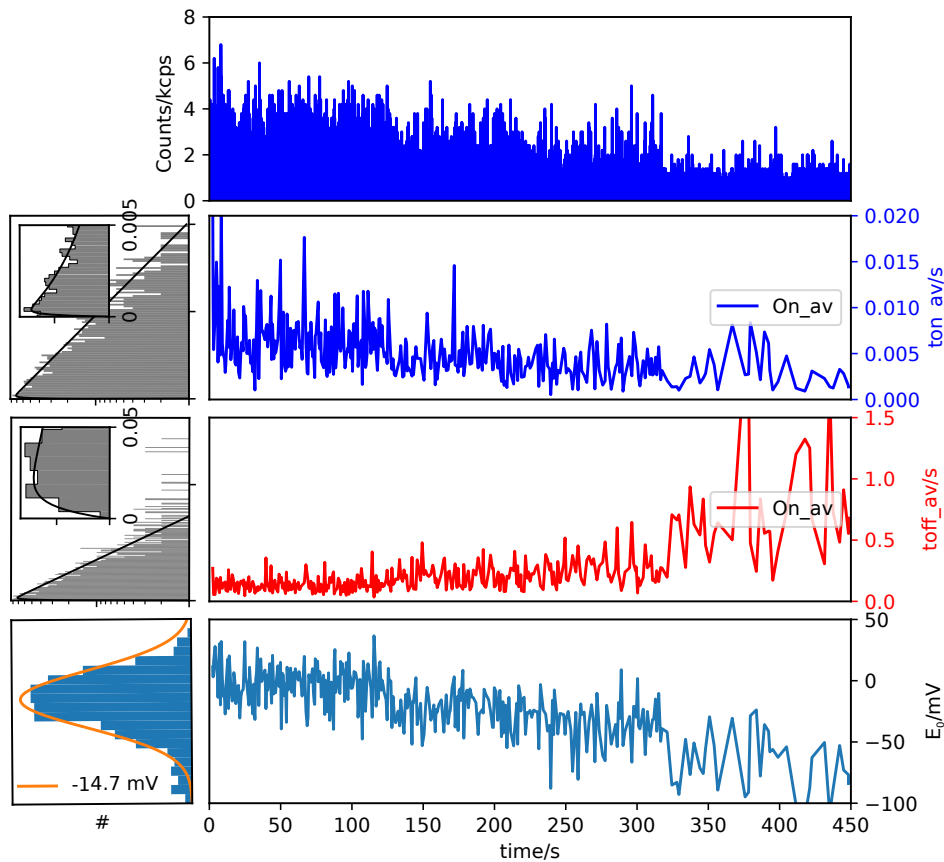
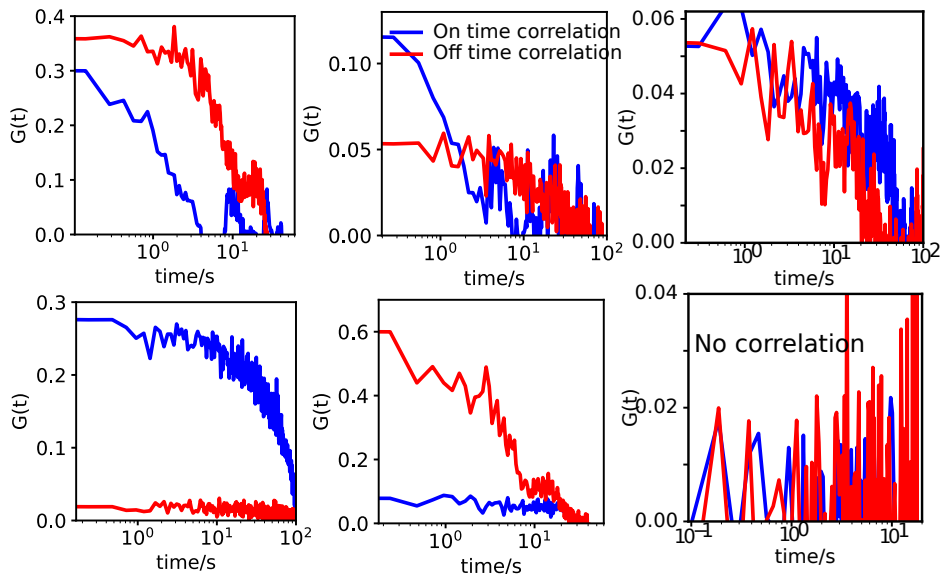


Figure 2.18. dynamic Point 20 75mVS105



**Figure 2.19. More examples of Dynamic correlation.**

## REFERENCES

- [1] W. E. Moerner and M. Orrit, *Illuminating single molecules in condensed matter*, *Science* **283**, 1670 (1999).
- [2] S. Weiss, *Fluorescence spectroscopy of single biomolecules*. *Science (New York, N.Y.)* **283**, 1676 (1999).
- [3] D. Magde, E. Elson, and W. W. Webb, *Thermodynamic fluctuations in a reacting system—measurement by fluorescence correlation spectroscopy*, *Phys. Rev. Lett.* **29**, 705 (1972).
- [4] H. Craighead, *Future lab-on-a-chip technologies for interrogating individual molecules*. *Nature* **442**, 387 (2006).
- [5] M. Levene, J. Korlach, S. Turner, M. Foquet, H. Craighead, and W. Webb, *Zero-mode waveguides for single-molecule analysis at high concentrations*. *Science (New York, N.Y.)* **299**, 682 (2003).
- [6] A. A. Kinkhabwala, Z. Yu, S. Fan, and W. Moerner, *Fluorescence correlation spectroscopy at high concentrations using gold bowtie nanoantennas*, *Chemical Physics* (2012), 10.1016/j.chemphys.2012.04.011.
- [7] D. Punj, M. Mivelle, S. B. Moparthi, T. S. v. Zanten, H. Rigneault, N. F. v. Hulst, M. F. García-Parajó, and J. Wenger, *A plasmonic ‘antenna-in-box’ platform for enhanced single-molecule analysis at micromolar concentrations*, *Nature Nanotechnology* **8**, 512 (2013).
- [8] H. Yuan, S. Khatua, P. Zijlstra, M. Yorulmaz, and M. Orrit, *Thousand-fold enhancement of single-molecule fluorescence near a single gold nanorod*. *Angewandte Chemie (International ed. in English)* **52**, 1217 (2013).
- [9] D. Punj, J. d. Torres, H. Rigneault, and J. Wenger, *Gold nanoparticles for enhanced single molecule fluorescence analysis at micromolar concentration*. *Optics express* (2013), 10.1364/oe.21.027338.
- [10] J. A. Schuller, E. S. Barnard, W. Cai, Y. C. Jun, J. S. White, and M. L. Brongersma, *Plasmonics for extreme light concentration and manipulation*. *Nature materials* **9**, 193 (2010).
- [11] P. Anger, P. Bharadwaj, and L. Novotny, *Enhancement and quenching of single-molecule fluorescence*. *Physical review letters* **96**, 113002 (2006).
- [12] A. Kinkhabwala, Z. Yu, S. Fan, Y. Avlasevich, K. Müllen, and W. Moerner, *Large single-molecule fluorescence enhancements produced by a bowtie nanoantenna*, *Nature Photonics* (2009), 10.1038/nphoton.2009.187.
- [13] G. Acuna, F. Möller, P. Holzmeister, S. Beater, B. Lalkens, and P. Tinnefeld, *Fluorescence enhancement at docking sites of dna-directed self-assembled nanoantennas*. *Science (New York, N.Y.)* **338**, 506 (2012).

- 2
- [14] M. P. Busson, B. Rolly, B. Stout, N. Bonod, and S. Bidault, *Accelerated single photon emission from dye molecule-driven nanoantennas assembled on dna*, *Nature Communications* (2012), **10.1038/ncomms1964**.
  - [15] P. Holzmeister, E. Pibiri, J. J. Schmied, T. Sen, G. P. Acuna, and P. Tinnefeld, *Quantum yield and excitation rate of single molecules close to metallic nanostructures*, (2014), **10.1038/ncomms6356**.
  - [16] S. Khatua, P. M. Paulo, H. Yuan, A. Gupta, P. Zijlstra, and M. Orrit, *Resonant plasmonic enhancement of single-molecule fluorescence by individual gold nanorods*. *ACS nano* (2014), **10.1021/nm406434y**.
  - [17] G. L. Liu, Y.-T. Long, Y. Choi, T. Kang, and L. P. Lee, *Quantized plasmon quenching dips nanospectroscopy via plasmon resonance energy transfer*, *Nature Methods* **4**, 1015 (2007).
  - [18] J. R. Lakowicz, *Radiative decay engineering: Biophysical and biomedical applications*, *Analytical Biochemistry* **298**, 1 (2001).
  - [19] E. Dulkeith, M. Ringler, T. A. Klar, J. Feldmann, A. M. Javier, and W. J. Parak, *Gold nanoparticles quench fluorescence by phase induced radiative rate suppression*. *Nano letters* **5**, 585 (2005).
  - [20] J. Seelig, K. Leslie, A. Renn, S. Kühn, V. Jacobsen, M. v. d. Corput, C. Wyman, and V. Sandoghdar, *Nanoparticle-induced fluorescence lifetime modification as nanoscopic ruler: demonstration at the single molecule level*. *Nano letters* **7**, 685 (2007).
  - [21] O. L. Muskens, V. Giannini, J. A. Sanchez-Gil, and J. G. Rivas, *Strong enhancement of the radiative decay rate of emitters by single plasmonic nanoantennas*. *Nano letters* **7**, 2871 (2007).
  - [22] M. Pelton, *Modified spontaneous emission in nanophotonic structures*, *Nature Photonics* **9**, 427 (2015).
  - [23] P. Zijlstra and M. Orrit, *Single metal nanoparticles: optical detection, spectroscopy and applications*, (2011).
  - [24] L. C. Estrada, P. F. Aramendía, and O. E. Martínez, *10000 times volume reduction for fluorescence correlation spectroscopy using nano-antennas*, *Optics Express* **16**, 20597 (2008).
  - [25] P. Ghenuche, M. Mivelle, J. d. Torres, S. B. Moparthi, H. Rigneault, N. F. V. Hulst, M. F. García-Parajó, and J. Wenger, *Matching nanoantenna field confinement to fret distances enhances förster energy transfer rates*. *Nano letters* **15**, 6193 (2015).
  - [26] D. Zhang, O. Neumann, H. Wang, V. M. Yuwono, A. Barhoumi, M. Perham, J. D. Hartgerink, P. Wittung-Stafshede, and N. J. Halas, *Gold nanoparticles can induce the formation of protein-based aggregates at physiological ph*. *Nano letters* **9**, 666 (2009).

- [27] G. Cooper, *The Cell: A Molecular Approach*, 2nd edn. *The Cell: A Molecular Approach*. Sunderland, MA (USA: Sinauer Associates, 2000).
- [28] F. Persson, J. Fritzsche, K. Mir, and M. Modesti, *Lipid-based passivation in nanofluidics*, (2012), [10.1021/nl204535h](https://doi.org/10.1021/nl204535h).
- [29] L. T. Iller, L. Iversen, M. Schmidt, C. Rhodes, H.-L. Tu, W.-C. Lin, and J. Groves, *Single molecule tracking on supported membranes with arrays of optical nanoantennas*, *Nano letters* **12**, 1717 (2012).
- [30] T. Lohmuller, S. Triffo, G. O'Donoghue, and Q. Xu, *Supported membranes embedded with fixed arrays of gold nanoparticles*, (2011), [10.1021/nl202847t](https://doi.org/10.1021/nl202847t).
- [31] E. Sackmann, *Supported membranes: Scientific and practical applications*, *Science* (1996), [10.1126/science.271.5245.43](https://doi.org/10.1126/science.271.5245.43).
- [32] E. T. Castellana and P. S. Cremer, *Solid supported lipid bilayers: From biophysical studies to sensor design*, *Surface Science Reports* **61**, 429 (2006).
- [33] P. S. Cremer and S. G. Boxer, *Formation and spreading of lipid bilayers on planar glass supports*, *The Journal of Physical Chemistry B* **103**, 2554 (1999).
- [34] R. P. Richter, R. Bérat, and A. R. Brisson, *Formation of solid-supported lipid bilayers: an integrated view*, *Langmuir* **22**, 3497 (2006).
- [35] B. Nikoobakht and M. A. El-Sayed\*, *Preparation and growth mechanism of gold nanorods (nr)s using seed-mediated growth method*, *Chemistry of Materials* (2003), [10.1021/cm020732l](https://doi.org/10.1021/cm020732l).
- [36] M. van de Kamp, F. C. Hali, N. Rosato, A. F. Agro, and G. W. Canters, *Purification and characterization of a non-reconstitutable azurin, obtained by heterologous expression of the pseudomonas aeruginosa azu gene in escherichia coli*, *Biochimica et Biophysica Acta (BBA) - Bioenergetics* **1019**, 283 (1990).
- [37] S. Nicolardi, A. Andreoni, L. C. Tabares, Y. E. v. der Burgt, G. W. Canters, A. M. Deelder, and P. J. Hensbergen, *Top-down fticr ms for the identification of fluorescent labeling efficiency and specificity of the cu-protein azurin*. *Analytical chemistry* **84**, 2512 (2012).
- [38] L. Langguth and F. A. Koenderink, *Simple model for plasmon enhanced fluorescence correlation spectroscopy*, *Optics Express* (2014), [10.1364/oe.22.015397](https://doi.org/10.1364/oe.22.015397).
- [39] R. Macháň and M. Hof, *Lipid diffusion in planar membranes investigated by fluorescence correlation spectroscopy*, (2010).
- [40] U. Kolczak, C. Dennison, A. Messerschmidt, and G. Canters, *Azurin and azurin mutants*, in *Handbook of Metalloproteins* (John Wiley & Sons, Ltd, 2006).
- [41] E. Vijgenboom, J. E. Busch, and G. W. Canters, *In vivo studies disprove an obligatory role of azurin in denitrification in pseudomonas aeruginosa and show that azu expression is under control of rpos and anr*, *Microbiology* **143**, 2853 (1997).

- [42] L. Langguth, C. I. Osorio, and A. F. Koenderink, *Exact analysis of nanoantenna enhanced fluorescence correlation spectroscopy at a mie sphere*, *The Journal of Physical Chemistry C* **120**, 13684 (2016).
- [43] M. v. d. Kamp, F. Hali, N. Rosato, A. Agro, and G. Canters, *Purification and characterization of a non-reconstitutable azurin, obtained by heterologous expression of the Pseudomonas aeruginosa azu gene in Escherichia coli*. *Biochimica et biophysica acta* **1019**, 283 (1990).
- [44] S. Nicolardi, A. Andreoni, L. C. Tabares, Y. E. v. d. Burgt, G. W. Canters, A. M. Deelder, and P. J. Hensbergen, *Top-down FTICR MS for the identification of fluorescent labeling efficiency and specificity of the Cu-protein azurin*. *Analytical chemistry* **84**, 2512 (2012).
- [45] A. Gupta, I. Nederlof, S. Sottini, A. W. J. W. Tepper, E. J. J. Groenen, E. A. J. Thomassen, and G. W. Canters, *Involvement of Tyr108 in the Enzyme Mechanism of the Small Laccase from Streptomyces coelicolor*, *Journal of the American Chemical Society* **134**, 18213 (2012).
- [46] W. Zhang, M. Calderola, B. Pradhan, and M. Orrit, *Gold Nanorod Enhanced Fluorescence Enables SingleMolecule Electrochemistry of Methylene Blue*, *Angewandte Chemie International Edition* **56** (2017), 10.1002/anie.201612389.
- [47] L. P. Watkins and H. Yang, *Detection of Intensity Change Points in Time-Resolved Single-Molecule Measurements*, *The Journal of Physical Chemistry B* **109**, 617 (2005).
- [48] R. I. Dave and N. P. Shah, *Effectiveness of ascorbic acid as an oxygen scavenger in improving viability of probiotic bacteria in yoghurts made with commercial starter cultures*, *International Dairy Journal* **7**, 435 (1997).
- [49] T. Cordes, J. Vogelsang, and P. Tinnefeld, *On the mechanism of trolox as antiblinking and antibleaching reagent*, *Journal of the American Chemical Society* **131**, 5018 (2009).
- [50] S. Kuznetsova, G. Zauner, R. Schmauder, O. A. Mayboroda, A. M. Deelder, T. J. Aartsma, and G. W. Canters, *A Förster-resonance-energy transfer-based method for fluorescence detection of the protein redox state*. *Analytical biochemistry* **350**, 52 (2006).
- [51] J. Davis, H. Burgess, G. Zauner, S. Kuznetsova, J. Salverda, T. Aartsma, and G. Canters, *Monitoring interfacial bioelectrochemistry using a FRET switch*. *The journal of physical chemistry. B* **110**, 20649 (2006).
- [52] J. M. Salverda, A. V. Patil, G. Mizzon, S. Kuznetsova, G. Zauner, N. Akkilic, G. W. Canters, J. J. Davis, H. A. Heering, and T. J. Aartsma, *Fluorescent cyclic voltammetry of immobilized azurin: direct observation of thermodynamic and kinetic heterogeneity*. *Angewandte Chemie (International ed. in English)* **49**, 5776 (2010).

- [53] N. Akkilic, F. v. d. Grient, M. Kamran, and N. J. M. Sanghamitra, *Chemically-induced redox switching of a metalloprotein reveals thermodynamic and kinetic heterogeneity, one molecule at a time*, *Chemical Communications* **50**, 14523 (2014).
- [54] H. P. Lu, L. Xun, and X. S. Xie, *Single-Molecule Enzymatic Dynamics*, *Science* **282**, 1877 (1998).
- [55] A. Patil and J. Davis, *Visualizing and tuning thermodynamic dispersion in metalloprotein monolayers*, *Journal of the American Chemical Society* **132**, 16938 (2010).
- [56] S. C. Kou, B. J. Cherayil, W. Min, B. P. English, and X. S. Xie, *Single-Molecule MichaelisMenten Equations*, *The Journal of Physical Chemistry B* **109**, 19068 (2005).
- [57] B. P. English, W. Min, A. M. v. Oijen, K. T. Lee, G. Luo, H. Sun, B. J. Cherayil, S. C. Kou, and X. S. Xie, *Ever-fluctuating single enzyme molecules: Michaelis-Menten equation revisited*. *Nature chemical biology* **2**, 87 (2006).